2021

Marangoni Propulsion of Active Particles

Saeed Jafari Kang
Michigan Technological University, sjafarik@mtu.edu

MARANGONI PROPULSION OF ACTIVE PARTICLES

By

Saeed Jafari Kang

A DISSERTATION

Submitted in partial fulfillment of the requirements for the degree of

DOCTOR OF PHILOSOPHY

In Mechanical Engineering–Engineering Mechanics

MICHIGAN TECHNOLOGICAL UNIVERSITY

2021

This dissertation has been approved in partial fulfillment of the requirements for the Degree of DOCTOR OF PHILOSOPHY in Mechanical Engineering–Engineering Mechanics.

Department of Mechanical Engineering–Engineering Mechanics

Dissertation Advisor:	*Dr. Hassan Masoud*
Committee Member:	*Dr. Fernando L. Ponta*
Committee Member:	*Dr. Kazuya Tajiri*
Committee Member:	*Dr. Kathleen A. Feigl*
Department Chair:	*Dr. William W. Predebon*

Dedication

To my parents, my brothers, and my fiancé

who always motivated me to follow my biggest dreams.

Acknowledgments

I would like to express my sincere gratitude to my advisor Dr. Hassan Masoud. I am forever grateful for his constructive criticism, invaluable advice, continuous support, and patience during my PhD study. I would like to also thank my dissertation committee Dr. Kathleen Feigl, Dr. Kazuya Tajiri, and Dr. Fernando Ponta for reviewing my dissertation.

I would like to extend my gratitude to the Department of Mechanical Engineering-Engineering Mechanics for honoring me with the prestigious Graduate Teaching Fellowship Award and giving me the opportunity to teach a fundamental course for undergraduate students. Also, I would like to thank Dr. Gordon Parker and Dr. Masoud for helping me in teaching.

I am also very thankful to my lab mates for guiding me through positive discussions, specifically, Dr. Vahid Vandadi, Dr. Esmaeil Dehdashti, and Mitch Timm. I would like to thank Dr. Johnathan Rothstein and Dr. Samrat Sur for their collaborations in our research and providing us with great results and advice.

Contents

List of Figures

List of Tables

Preface

This dissertation includes contents that were previously published as journal articles. The full citation of the papers are:

- Reverse Marangoni surfing, V. Vandadi, S. Jafari Kang, and H. Masoud, *Journal of Fluid Mechanics* 811, 612–621 (2017);

- Forward, reverse, and no motion of Marangoni surfers under confinement, S. Jafari Kang, S. Sur, J. P. Rothstein, and H. Masoud, *Physical Review Fluids* 5, 084004 (2020).

Both studies were collaborative. In the first one, all authors contributed to the theoretical analyses, numerical simulations, and writing of the manuscript. And, in the second one, the author of this dissertation (Saeed Jafari Kang) and his advisor (Dr. Hassan Masoud) were the primary contributors to the numerical simulations and writing of the manuscript, while the remaining authors were mainly responsible for conducting the experiments.

Abstract

We study the surfing motion of active particles located at a flat liquid-gas interface. The particles create and maintain a surface tension gradient by asymmetrically discharging a surface tension-reducing agent. We employ theory and numerical simulation to investigate the Marangoni propulsion of these active surfers. First, we use the reciprocal theorem to establish a relationship between the propulsion speed and the release of the active chemical. This theoretical relation is utilized to examine the effect of wall confinement and geometry on the Marangoni-driven motion of active particle when the inertial effects are negligible and when the transports of the released agent is dominated by diffusion. Contrary to what might be the usual expectation, we find that the surfers may propel in the lower surface tension direction depending on their geometry and proximity to the bottom of the liquid layer. We then extend our theory beyond the Stokes regime with the aid of the perturbation theory and calculate the leading-order corrections to the propulsion speed due to the advective transport of momentum and mass when the Reynolds and Péclet numbers (denoted by Re and Pe, respectively) are small, but finite.

Next, we develop a computational framework that enables us to study the effects of intermediate and large Re and Pe on the propulsion speed. Our numerical approach is validated against theory and available experimental data. Interestingly, our simulations reveal that the normalized propulsion speed initially increases with increasing Re and Pe from zero. It then reaches a maximum and afterward sharply declines when

Re or Pe becomes large. That there exist certain intermediate Reynolds and Péclet numbers at which the Marangoni propulsion reaches a peak is a new finding that can guide engineers to design Marangoni surfers with superior performance.

We also numerically analyze the translational stability of Marangoni surfers of spherical shape. An overset-grid is adopted to carry out the simulations. We demonstrate that a Marangoni surfer can retain its stability at higher Reynolds numbers relative to the same surfer moving at an interface with no Marangoni effect present. Lastly, we computationally investigate the change in the mobility of the surfers as a result of the depth of the liquid layer. We consider the motion of thin cylindrical disks and oblate spheroids for a wide range of release rates and diffusivity of the exuded chemical species, that control the effective Reynolds and Péclet numbers. We show that indeed the surfers can undergo a forward, a backward, or an arrested motion. We also identify the links between these modes of mobility and the forces acting on the surfers as well as the flow structure in their vicinity. Rather unexpectedly, we discover that negative pressure is the primary contributor to the fluid force experienced by the surfer and that this suction force is mainly responsible for the reverse Marangoni propulsion. Overall, our findings substantially improve the current understanding of the Marangoni-driven motion of active particles at liquid-gas interfaces and pave the way for engineering future miniature surfing robots.

Chapter 1: Introduction

1.1 Background and Motivations

Self-propelled microdevices powered by converting chemical energy into mechanical work bring to bear functionalities that resemble those of microorganisms. These miniature robots are thus promising candidates for targeted drug delivery, microsurgery, self-assembly, and microfluidic manipulation [1, 2]. Thanks to the recent advances in the MEMS/NEMS technology, researchers have designed and tested a wide variety of swimming microrobots, many of them biomimetic, to carry out prescribed tasks in microfluidic systems [3–12]. However, despite recent notable progress in creating microswimmers, the development of microscopic machines capable of surfing on fluidic interfaces is still at its infancy.

The transport of interface-trapped particles due to self-generated surface tension gradients appears frequently in man-made and biological systems. Arguably, the most basic human-made example is the camphor boat [13, 14], where the gradual dissolution of a camphor piece attached to the back of the boat creates a for/aft surface tension asymmetry (with associated Marangoni flows) that leads to the self-propulsion of the craft (see figure 1.1a). Miniature analogues of this very simple Marangoni surfer

have been created recently [15–30] with the ultimate goal of designing programmable surfing robots for microfluidic manipulation, self-assembly, and targeted drug delivery. These tiny Marangoni surfers can potentially execute missions that are currently very difficult or even impossible to accomplish [1, 2, 6, 31].

The Marangoni propulsion emerges in biological systems as well. For instance, there are water-walking insects, such as Dianous (a rove beetle) and Velia (a small water strider) that secrete surface-active materials (see figure 1.1b) to boost their walking speed in emergency situations [32–35]. Marangoni propulsion have also been reported as the primary mechanism for the rapid interfacial migration of bacterial swarms towards nutrient-rich regions for further colonization [36–39]. These studies have suggested that the signaling molecules exuded by the surface-associated bacteria such as Pseudomonas aeruginosa are also active agents that locally alter the surface tension. Fighting these infectious microrganisms by antibiotics often involves hampering their Marangoni-driven collective dynamics responsible for their colonization.

Despite its ubiquity and significance in many important contexts, Marangoni propulsion of particles remains heavily understudied. This perhaps stems from the presence of additional complexities that arise due to the coupling between the dynamics of the immersing interface and fluid flows, on one hand, and the locomotion of the particles and transport of released chemical species or heat on the other hand. The current lack of fundamental understanding in this area impedes the development of advanced Marangoni surfers for emerging engineering applications and also makes

(a) (b)

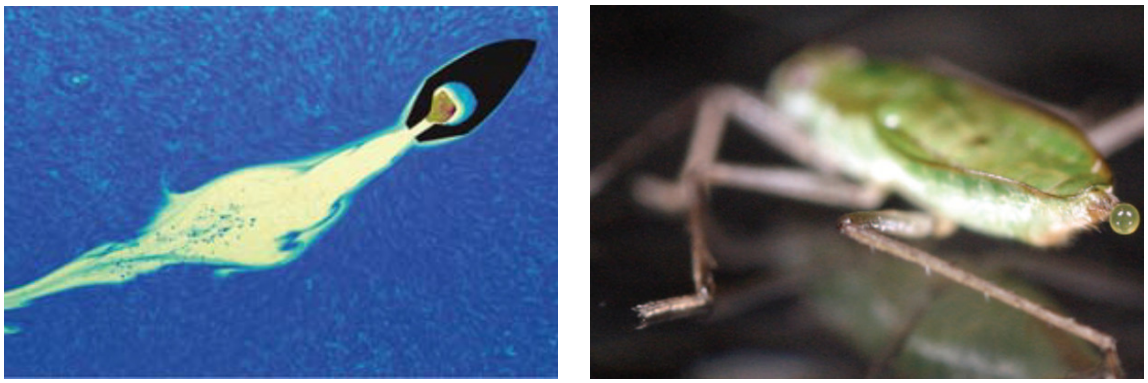

Figure 1.1: Examples of Marangoni propulsion in man-made and natural systems (adopted from [35, 40]). The figures visualize (a) the concentration of released chemical agents in the wakes of a surfing camphor boat and (b) a small water strider (Velia) excreting an active fluid from its anus.

it very challenging, if not impossible, to uncover the role of self-induced Marangoni stresses in the colonization and locomotion of biological organisms.

1.2 Previous Studies

Investigations into the propulsion of floating objects triggered by an auto-modulation of nearby interfacial stresses date back, at least, to the pioneering work of Lord Rayleigh, in the late 19$^{\text{th}}$ century, on the motion of camphor scrapings along a water-air interface [13]. Since then, there have been several other attempts to examine the motion of active particles of various shapes and sizes that self-propel at fluidic interfaces by creating a gradient of surface tension in their immediate vicinity [9, 14–27, 29, 30, 41–71]. Among the experimental studies, Bassik et al. [15] considered the translational and rotational motion of ethanol-soaked poly-N-isopropylacrylamide gels

at a water-air interface. Their measurements indicated that the propulsion velocity is linearly related to the spreading speed of ethanol. They also observed that the maximum rotational velocity of the gels is inversely related to their linear dimensions. In a proof-of-concept study, Zhang et al. [22] showed the feasibility of using a depolymerization reaction to power the surfing motion of objects ranging from micrometer to centimeter scales. They observed that microscale particles achieve speeds of up to 660 body lengths per second. Also, Maggi et al. [9] designed a continuously rotating microgear that uses the principle of Marangoni propulsion to convert light into mechanical work. In this design, the light absorbed by the gear sitting on a water-air interface locally changes the surface tension, which, in turn, leads to the rotation of the gear. The researchers concluded that the Marangoni propulsion is one of the strongest mechanisms for light actuation at small scales. More recently, Sur et al. [70] investigated the dynamics of disk-shaped Marangoni surfers dip-coated on one side by a layer of either soap or isopropyl alcohol. Conducting particle tracking and particle image velocimetry (PIV) measurements, they found that the surfers follow a straight steady-state motion at low to moderate speeds, and observed a transition from translational to orbital motion beyond a critical Reynolds number defined based on the propulsion speed of the surfer.

Theoretical efforts to understand the Marangoni propulsion of active surfers include the works of Lauga and Davis [48] and Würger [51], where the propulsion speeds of, respectively, disk-shaped and spherical particles are analytically calculated in the

absence of inertia. The derivations involve direct solution of the Stokes equations for the flow of the liquid. The calculations showed that the translational propulsion speed is independent of the size of the particle. In the same context, Masoud and Stone [52] used the reciprocal theorem [72] to bypass detailed calculation of the flow field and derived closed-form expressions for the speed of active oblate and prolate spheroids. There also exist studies on the collective motion of surfers. For instance, Masoud and Shelley [53] considered the dynamics of a flock of chemically active surfers. Their linear stability analysis and numerical simulations using a Fourier pseudo-spectral method revealed that, if the particles' activity locally raises the surface tension, surface flows of chemical surfers can cause them to clump together – a phenomenon reminiscent of the self-aggregation of slime mold colonies.

1.3 Objectives and Outline

Our literature survey in the previous section reveals that the state-of-the-art in the area of Marangoni propulsion of active surfers currently suffers from several shortcomings. For example, it is not clear how the inertial effects and the advective transport of the chemical agent or heat alter the propulsion speed. The effects of particle geometry and interface deformation are not well understood either. Also, there is a lack of basic knowledge about the influence of system scale confinement, such as boundaries and obstacles, on the propulsion dynamics of particles. Such knowledge is critically needed as in many applications the Marangoni propulsion takes place in the presence of a

confining solid boundary. More importantly, there is no solid study on the stability characteristics of Marangoni surfers. This information is essential for determining the applicability range of the surfers for various applications.

The main objective of this dissertation is to address some of these deficiencies by systematically investigating the Marangoni surfing of interface-bound particles using a combination of theoretical calculations and numerical simulations. Here, we aim to (i) characterize the Marangoni propulsion of single particles in unbounded domains, (ii) investigate the influence of confinement on the propulsion dynamics of particles, and (iii) analyze the stability of self-propelled surfers.

The remaining chapters of this dissertation are organized as follows. In the next chapter, we theoretically examine the Marangoni-driven motion of surfers by introducing a reciprocal theorem-based formulation for the propulsion speed. Then, we describe the computational method developed for simulating the Marangoni propulsion (§3). In chapter §4, we present our findings for the optimum speed and translational stability of the Marangoni propulsion and its variations under confinement. We conclude with chapter §5, where we summarize our results and discuss future research directions.

Chapter 2: A Reciprocal Theorem for Marangoni Propulsion

2.1 Introduction

In this chapter, we theoretically study the propulsion speed of Marangoni surfers at steady state condition. Specifically, we consider two cases: (i) surfing atop a finite layer of liquid in the absence of advective momentum and mass transport (i.e., when $\mathrm{Re} = \mathrm{Pe} = 0$) and (ii) Marangoni propulsion at non-zero (but small) Reynolds and Péclet numbers when the liquid layer is very deep. The results of our analyses, which are based on the reciprocal theorem (see, e.g., [72]), motivate the numerical calculations presented in chapter §3.

2.2 The Case of Zero Reynolds and Péclet Numbers

Consider a particle located at a flat liquid-gas interface, at $z = 0$, sitting above a layer of Newtonian fluid, with constant density ρ and viscosity μ (see Fig. 2.1). The particle translates with the velocity $\boldsymbol{U} = U\boldsymbol{e}$ due to a non-uniformity in the surface tension γ arising from an asymmetric release of a surface-active chemical species (with diffusivity $\mathcal{D}$) from the particle's surface. Here, $\boldsymbol{e}$ is the unit vector in the direction

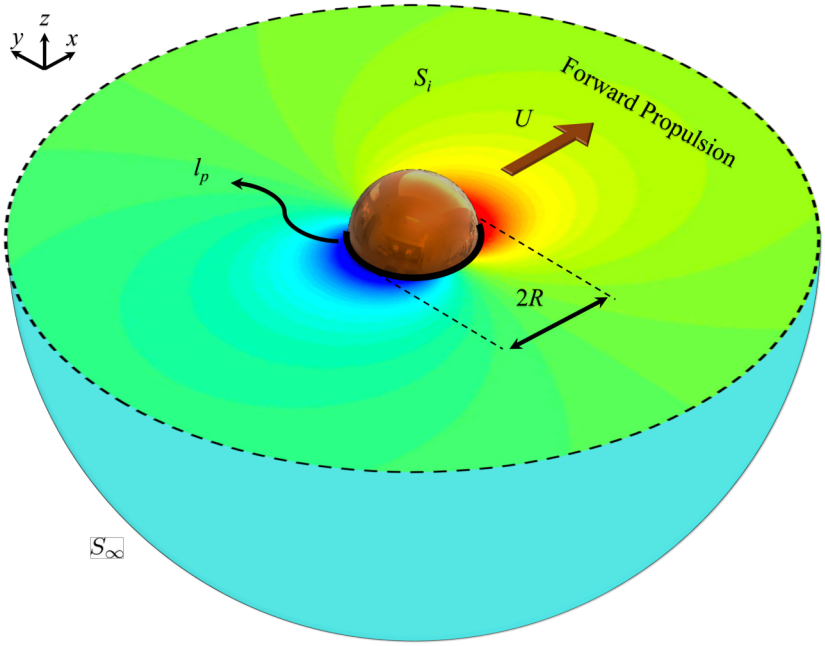

Figure 2.1: Schematic of a Marangoni surfer propelling atop a semi-infinite liquid layer. The color map at the interfaces represent the surface tension distribution resulting from the release of a chemical species from the surfer. S_i and l_p denote, respectively, the liquid-gas interface and three-phase contact line pinned to the particle at 90° contact angle. The dashed enclosing contour and S_∞ show the lack of outer boundaries.

of motion.

To reduce the complexity of the calculations, the following justifiable assumptions are made: (i) the liquid-gas interface is flat; (ii) the three-phase contact line is pinned at a 90° contact angle; (iii) the released chemical species is soluble into the bulk of the liquid layer and its three-dimensional transport is dominated by diffusion; (iv) gravitational and inertial effects are negligible, (v) the liquid is Newtonian with constant density and viscosity that are unaffected by the presence of the solute; (vi) the surface tension of the liquid varies linearly with the concentration of the chemical species; and (vii) the particle undergoes a pure translational motion along a straight

line parallel to the interface.

A typical experimental setup for which the assumptions are valid is an aqueous system with particles of diameter $D \sim 1\,\mu$m and propulsion speed $U \sim 1\,\mu$m/s that produce a chemical species with a diffusion constant $\mathscr{D} \sim 10^{-10}\,\mathrm{m}^2/\mathrm{s}$. The Capillary, Péclet, and Reynolds numbers of this system are, respectively, $\mathrm{Ca} = \mu U/\gamma_0 \sim 10^{-8}$, $\mathrm{Pe} = DU/\mathscr{D} \sim 10^{-2}$, and $\mathrm{Re} = \rho DU/\mu \sim 10^{-6}$. The assumptions are similarly valid for an aqueous system with optically heated particles of diameter $D \sim 10\,\mu$m whose propulsion speed is $U \sim 10\,\mu$m/s. Here, the corresponding dimensionless numbers are $\mathrm{Ca} \sim 10^{-7}$, $\mathrm{Pe} = DU/\alpha \sim 10^{-3}$, and $\mathrm{Re} \sim 10^{-4}$. The non-dimensional numbers are calculated based on the water properties at room condition (i.e. density $\rho = 997.0479\,\mathrm{kg/m}^3$, viscosity $\mu = 8.90 \times 10^{-4}\,\mathrm{N{\cdot}s/m}^2$, thermal diffusivity $\alpha = 0.143 \times 10^{-6}\,\mathrm{m}^2/\mathrm{s}$, and surface tension $\gamma_0 = 71.97 \times 10^{-3}\,\mathrm{N/m}$). In both setups, the surface tension is strong enough to keep the interface flat ($\mathrm{Ca} \ll 1$), the primary mode of heat and mass transfer is diffusion ($\mathrm{Pe} \ll 1$), and the flow is creeping ($\mathrm{Re} \ll 1$).

2.2.1 Derivation of the Propulsion Speed

Suppose $\boldsymbol{u}$ and $\boldsymbol{\sigma}$ are, respectively, the velocity and stress fields, in $z \leq 0$, corresponding to the Marangoni-driven motion of the particle. Let $\hat{\boldsymbol{u}}$ and $\hat{\boldsymbol{\sigma}}$ denote, respectively, the velocity and stress fields corresponding to the translation with the velocity $\hat{\boldsymbol{U}} = \hat{U}\boldsymbol{e}$ of an identical particle at an interface with no surface tension gradients. These fields are free of contact-line singularities, as the particle motion is

limited to pure translation [73, 74]. Hence, according to the reciprocal theorem (see, e.g., [72]),

$$\begin{aligned}&\int_{S_p} (\boldsymbol{n}\cdot\boldsymbol{\sigma})\cdot\hat{\boldsymbol{u}}\,\mathrm{d}S + \int_{S_i} (\boldsymbol{n}\cdot\boldsymbol{\sigma})\cdot\hat{\boldsymbol{u}}\,\mathrm{d}S\\ =&\int_{S_p} (\boldsymbol{n}\cdot\hat{\boldsymbol{\sigma}})\cdot\boldsymbol{u}\,\mathrm{d}S + \int_{S_i} (\boldsymbol{n}\cdot\hat{\boldsymbol{\sigma}})\cdot\boldsymbol{u}\,\mathrm{d}S,\end{aligned} \tag{2.1}$$

where S_p is the wetted area of the particle, S_i represents the liquid-gas interface (see Fig. 2.1), and $\boldsymbol{n}$ is the unit vector outward normal to S_p and S_i. When the fluid domain is only confined by the interface (see Fig. 2.1), the integrals over the bounding surface at infinity (denoted by S_∞) are zero since the velocities decay at least as fast as the inverse of distance in the far field. If the fluid domain is bounded from below or sides by walls (see, e.g., Fig. 2.2), the integrals over those boundaries also vanish due to the zero-velocity boundary condition.

Owing to the no-slip condition, $\boldsymbol{u} = U\boldsymbol{e}$ and $\hat{\boldsymbol{u}} = \hat{U}\boldsymbol{e}$ on S_p. Also, the components of $\boldsymbol{u}$ and $\hat{\boldsymbol{u}}$ normal to the interface are zero as no fluid exchange takes place there. The balance of shear stress at the interface requires that

$$(\boldsymbol{n}\cdot\boldsymbol{\sigma})\cdot\hat{\boldsymbol{u}} = -\nabla_s\gamma\cdot\hat{\boldsymbol{u}} \quad \text{and} \quad (\boldsymbol{n}\cdot\hat{\boldsymbol{\sigma}})\cdot\boldsymbol{u} = 0 \tag{2.2}$$

on S_i, where ∇_s is the surface gradient operator. Since no net external force is applied on the particle, the viscous force $\int_{S_p} \boldsymbol{n}\cdot\boldsymbol{\sigma}\,\mathrm{d}S$ exerted on S_p is balanced by the surface tension force $F_{st}\,\boldsymbol{e} = \int_{\ell_p} \gamma\boldsymbol{t}\,\mathrm{d}\ell$ acting along the three-phase contact line ℓ_p, where $\boldsymbol{t}$ is the unit vector tangent to S_i and normal to ℓ_p (see Figs. 2.1 and 2.2). Taking the

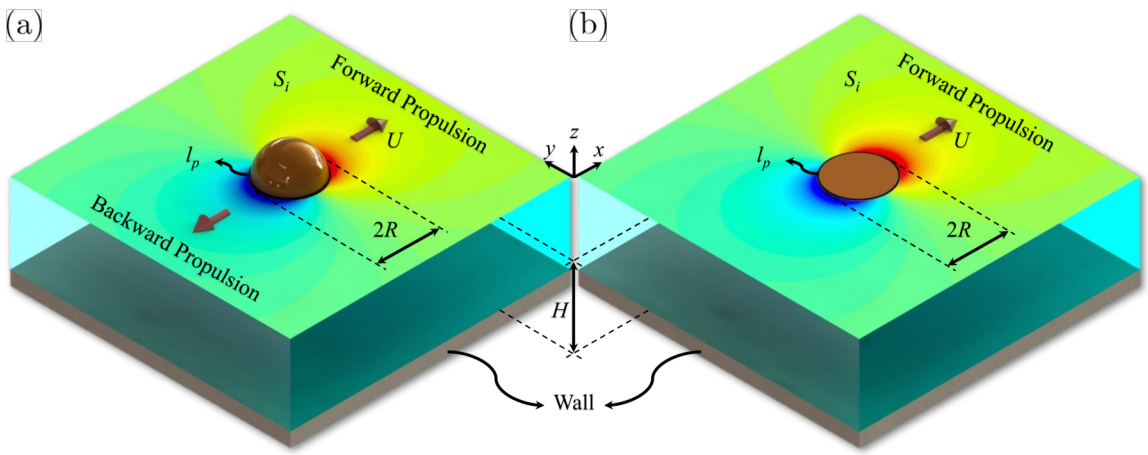

Figure 2.2: Marangoni propulsion of (a) spherical and (b) disk-shaped particles at a flat interface above a liquid layer of finite depth. The color maps at the interfaces represent the surface tension distribution around the surfers. S_i and l_p denote, respectively, the liquid-gas interface and three-phase contact line pinned to the particle at 90° contact angle. The translation towards the higher surface tension direction is regarded as the forward propulsion.

above relations into account, Eq. (2.1) reduces to

$$U = \frac{\hat{U}}{\hat{F}_d}\left(F_{st} + F_{_M}\right), \tag{2.3}$$

where $-\hat{F}_d\,\boldsymbol{e} = \int_{S_p} \boldsymbol{n}\cdot\hat{\boldsymbol{\sigma}}\,\mathrm{d}S$ is the fluid drag that the translating particle would have experienced in response to its motion at the interface had there been no Marangoni effect and $F_{_M} = \int_{S_i}(\hat{\boldsymbol{u}}/\hat{U})\cdot\nabla_s\gamma\,\mathrm{d}S$ is the contribution of the Marangoni flow. In the conventional approach, calculating U entails solving the Stokes flow equations for $\boldsymbol{u}$ subject to the no-slip and Marangoni stress boundary conditions (see, e.g., [48, 51]). The use of the reciprocal theorem, instead, allows us to obtain U by just having $\hat{\boldsymbol{u}}$ (see Eq. (2.3)), which is analytically easier to calculate.

2.2.2 Propulsion Speed of Spheres and Disks

We now apply Eq. (2.3) to determine U for spherical and disk-shaped particles moving atop a liquid layer that is bounded by a solid wall at $z = -H$ (see Fig. 2.2). Conveniently, $\hat{\boldsymbol{u}}$ is already derived for the creeping motion of spheres and disks between parallel plates [75, 76]. Note that when the particle is located at an equal distance from the walls, due to the symmetry, the velocity fields obtained by Ganatos et al. [75] and Davis [76] are identical to those generated by the translation of the same particle along a flat liquid-gas interface sitting above a liquid layer bounded by a solid boundary. This argument holds when the Capillary number is very low, which indicates that the deflection of the interface due to the pressure distribution along the free surface can be ignored. The $\mathrm{Ca} \ll 1$ condition is a stronger constraint when the fluid layer is shallow.

Without loss of generality, we set the direction of motion to $\boldsymbol{e} = \boldsymbol{e}_x$ (see Fig. 2.2). Hence, following the solution of Ganatos et al. [75] for a sphere of radius R, the in-plane components of velocity $\hat{\boldsymbol{u}}$ in the spherical coordinates (r, θ, φ) at the interface $(\theta = 0)$ are

$$\frac{\hat{u}_r}{\hat{U}} = \cos\varphi \sum_{m=1}^{\infty} \sum_{n=1}^{3} A_{m,n}\left(H/R\right) F_{m,n}\left(r/R, H/R\right), \tag{2.4a}$$

$$\frac{\hat{u}_\varphi}{\hat{U}} = \sin\varphi \sum_{m=1}^{\infty} \sum_{n=1}^{3} A_{m,n}\left(H/R\right) G_{m,n}\left(r/R, H/R\right), \tag{2.4b}$$

where $\{A_{m,n}\}$ are functions of H/R obtained via a collocation technique, and $\{F_{m,n}\}$

and $\{G_{m,n}\}$ are functions of r/R and H/R (see Eqs. (2.6), (2.10), (2.24), and Appendix C of Ganatos et al. [75]). Also, according to Davis [76], the velocity components at $z = 0$ in the cylindrical coordinates (r, φ, z) for a disk of zero thickness and the same radius R are

$$\frac{\hat{u}_r}{\hat{U}} = R^2 \cos\varphi \left[\frac{\partial}{\partial r} \left(\frac{\Phi_{z,0}}{r} \right) + \frac{\Gamma_0}{r^2} \right], \tag{2.5a}$$

$$\frac{\hat{u}_\varphi}{\hat{U}} = R^2 \sin\varphi \left[-\frac{\Phi_{z,0}}{r^2} - \frac{\partial}{\partial r} \left(\frac{\Gamma_0}{r} \right) \right], \tag{2.5b}$$

where Φ and Γ are functions of r/R, z/R, and H/R with $\Gamma_0 = \Gamma|_{z=0}$ and $\Phi_{z,0} = R\,\partial\Phi/\partial z|_{z=0}$ (see equations (4.7), (4.18), (4.19), (4.22), and (4.23) of Davis [76]).

Following our assumption, the surface tension changes linearly with the concentration of the surface-active agent at the interface as

$$\gamma = \gamma_0 + \alpha\, c|_{z=0}, \tag{2.6}$$

where γ_0 and α are constants [77, 78]. Here, c denotes the steady-state concentration field that satisfies the Laplace equation $\nabla^2 c = 0$. This is true when the dominant mechanism of transport is diffusion (i.e., Pe = 0). Inspection of Eqs. (2.4) and (2.5) reveals that only the first harmonic modes of φ appear in $\hat{\boldsymbol{u}}$. This, in conjunction with (2.6), indicates that only the terms proportional to $\cos\varphi$ in multipole expansion of c contribute to the integral in (2.3). Retaining just the leading-order term in powers of R/r that has a non-zero contribution to U, we can write

$$c|_{z=0} = 2\,B \sum_{n=-\infty}^{\infty} \frac{r\cos\varphi}{R\left[(r/R)^2 + (2nH/R)^2\right]^{3/2}} + \ldots, \tag{2.7}$$

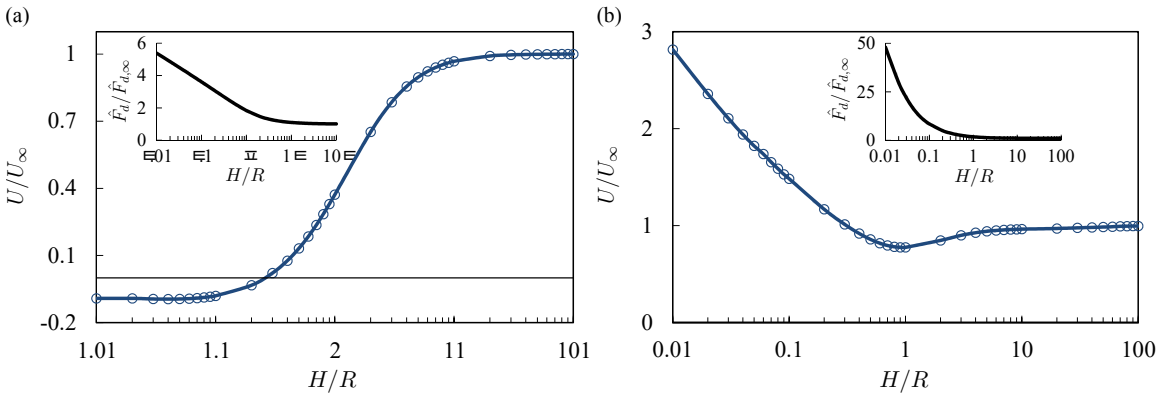

Figure 2.3: The normalized propulsion speed U/U_∞ as a function of the thickness of the fluid layer H/R for (a) spherical and (b) disk-shaped particles. The insets in (a) and (b) show the variation of $\hat{F}_d/\hat{F}_{d,\infty}$ (normalized Stokes drag experienced by the particle translating at an interface with no surface tension gradients) versus H/R obtained from the solutions of Ganatos et al. [75] and Davis [76]. Here, the speed and drag corresponding to a semi-infinite fluid layer ($H/R \to \infty$) are denoted, respectively, by U_∞ and $\hat{F}_{d,\infty}$, whose values for spheres and disks are shown in Fig. 2.4. Also, the thin solid line in subfigure (a) corresponds to $U = 0$.

where B is a constant. Equation (2.7) is derived using the method of images assuming that $\boldsymbol{n} \cdot \boldsymbol{\nabla} c = 0$ at the interface and on the wall.

Substituting Eqs. (2.4)-(2.7) into Eq. (2.3), we obtain the propulsion speed of active spheres and disks. Figure 2.3 shows the plots of U/U_∞ versus H/R, where U_∞ denotes U for a semi-infinite fluid layer. We see that when the fluid layer is very deep ($H/R \geq 100$) the speed is within 2% of its asymptotic value for both cases considered. On the other hand, when the fluid layer is shallow ($H/R < 1.5$), we see distinctly different behaviors for spheres and disks. Notably, we find that spheres come into a halt at a certain distance from the wall ($H/R \simeq 1.25$), closer than which they propel in the lower surface tension direction (see Fig. 2.3a). This contradicts the default notion that Marangoni surfers self-propel towards the direction with a higher surface

tension.

According to Eq. (2.3), the sign of U is set by the competition between two opposing influences, namely the net surface tension force acting along the three-phase contact line and the Marangoni flow induced by the surface tension gradients that are represented by F_{st} and F_{M}, respectively. Note that $\hat{F}_d/\hat{U}$ is always positive (see the insets in Fig. 2.3). Thus, if the contribution of F_{M} is neglected, U always has the same sign as F_{st}, meaning that the particles are always pulled towards the higher surface tension direction. This could be the origin of the common perception about the direction of Marangoni propulsion.

The effect of the confinement on the propulsion speed of disks is also noteworthy. Figure 2.3b shows that the speed of active disks increases logarithmically as $H/R \to 0$. Here, the speed surge in shallow depths stems from the fact that the solid wall is insulated. The combination of adiabatic condition and narrow layer results in steeper temperature gradients, which further augment F_{st} over F_{M}. Ultimately, the overall gain of $(F_{st} + F_{M})$ outweighs the increase of $\hat{F}_d$ (see Figs. 2.3b and Eq. (2.3)). Remember that, here, we have assumed that B in Eq. (2.7) is constant, which implies that the release rate of the chemical species remains unchanged as H/R decreases.

2.2.3 Propulsion Speed of Oblate Spheroids

Thanks to the reciprocal theorem, we have so far analytically calculated U for spheres and disks. Obtaining U in a similar manner for general oblate spheroids requires a

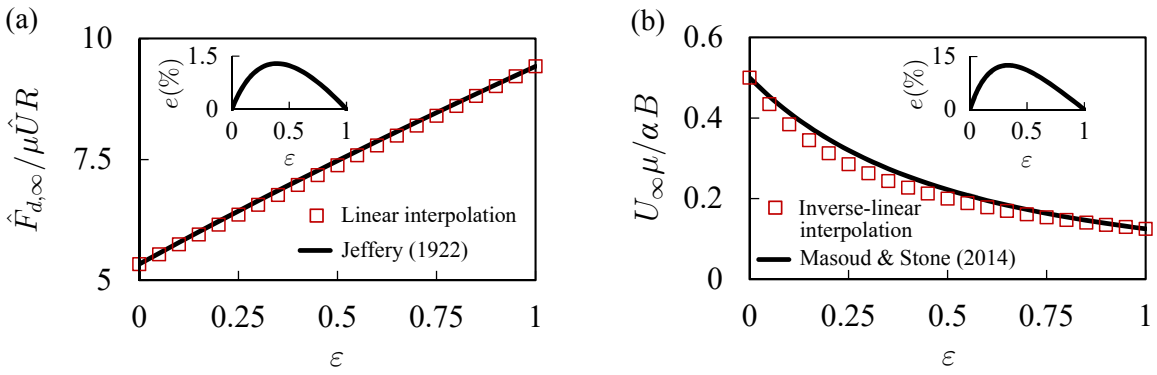

Figure 2.4: Comparison between the exact and approximate results for oblate spheroidal particles translating at an interface above a semi-infinite layer of fluid ($H/R \to \infty$). (a) The variation of non-dimensional drag $\hat{F}_{d,\infty}/\mu\hat{U}R$ versus the particle aspect ratio ε. (b) The dimensionless propulsion speed of thermally active spheroids $U_\infty\mu/K_{_T}B_{_T}$ as a function of ε. The solid lines represent exact analytical results whereas square symbols depict approximate values obtained via interpolations between the results for spheres and disks. The insets show the relative error of the approximations.

closed-form expression for $\hat{\boldsymbol{u}}$, which is not readily available. In what follows, we propose an approximate method for calculating the propulsion speed of oblate spheroids based on our results for spheres and disks.

Consider an oblate spheroid translating at an interface above a semi-infinite layer of fluid ($H/R \to \infty$). If we plot the analytically-known drag $\hat{F}_{d,\infty}$ as a function of the particle aspect ratio ε (see Fig. 2.4a), we observe that the drag changes almost linearly with the aspect ratio (see also the Appendix of [79]). In fact, the curve can be approximated extremely well by

$$\hat{F}^{D}_{d,\infty} + \varepsilon\left(\hat{F}^{S}_{d,\infty} - \hat{F}^{D}_{d,\infty}\right), \tag{2.8}$$

where the superscripts S and D denote the values for sphere ($\varepsilon = 1$) and disk ($\varepsilon = 0$), respectively. The inset in Fig. 2.4a shows that the maximum relative error is

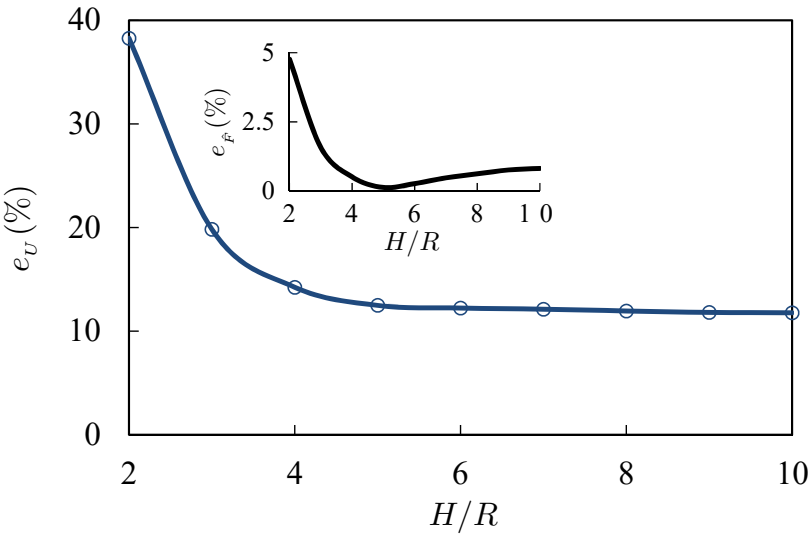

Figure 2.5: Comparison between the numerical and approximate results for oblate spheroidal particles of aspect ratio $\varepsilon = 0.4$. The main curve shows the relative approximation error e_U for the propulsion speed of the thermally active oblate at different distances from the wall H/R. The inset shows the relative error for the drag $e_{\hat{F}}$ as a function of H/R.

1.3% belonging to $\varepsilon = 0.4$. That the particle resistance varies quasi-linearly with the aspect ratio suggests that the particle mobility (i.e. U) changes inverse-linearly with ε. Remarkably, we find that the curves of U_∞ versus ε for spheroids are closely represented by (see Fig. 2.4b)

$$\left[\frac{1}{U_\infty^D} + \varepsilon\left(\frac{1}{U_\infty^S} - \frac{1}{U_\infty^D}\right)\right]^{-1}. \tag{2.9}$$

Again, the maximum error occurs at $\varepsilon = 0.4$ and its magnitude is 12.5% (see the inset of Fig. 2.4b).

These observations strongly recommend employing the same type of interpolations used in (2.8) and (2.9) for approximating the drag $\hat{F}_d$ and propulsion speed U of oblate spheroidal particles in the presence of the confining solid boundary. To test

the validity of such estimations, we numerically calculate $\hat{F}_d$ and U for $\varepsilon = 0.4$ and compare the results with those obtained by interpolating between the data presented in Fig. 2.3. Our numerical approach integrates a boundary singularity method with the (infinite) image technique [80]. Also, we choose $\varepsilon = 0.4$ because, very likely, the error is maximum at this aspect ratio (see the insets of Fig. 2.4). Indeed, we find that the approximations for U are reasonably accurate, particularly for $H/R \geq 4$ (see Fig. 2.5). The interpolation performs even better for $\hat{F}_d$, where the error is below 5% for $H/R \geq 2$.

Overall, our calculations indicate that depending on the geometry and degree of confinement, the surfers may propel forward in the higher surface tension direction or propel backward in the reverse direction. Knowing that the direction of propulsion is altered by a change in the surrounding boundary can be harnessed for designing smart surfing robots capable of sensing their environment. Here, we only applied our theory to particles with 90° contact angle (i.e., half-submerged). However, the propulsion speed of a particle with a contact angle other than 90° can be estimated by calculating the speed of a half-submerged oblate spheroid with the same protrusion length to the liquid phase and the same contact line radius. It has been shown that the fluid drags experienced by the two particles are closely comparable (see, e.g., [79]).

2.3 The Limit of Small, But Finite, Reynolds and Péclet Numbers

In the previous section, we studied the Marangoni propulsion subject to a number of simplifying assumptions including $\mathrm{Re} = \mathrm{Pe} = 0$. As a natural next step, here, we examine the limits of small (but finite) Reynolds and Péclet numbers ($\mathrm{Re} \ll 1$ and $\mathrm{Pe} \ll 1$), while leaving the remaining assumptions unchanged. We, again, use the reciprocal theorem to obtain a formula for the propulsion speed. The derivation proceeds as follows.

Consider a surfer of arbitrary shape and let $\boldsymbol{r} = x\boldsymbol{e}_x + y\boldsymbol{e}_y + z\boldsymbol{e}_z$ be the position vector with $r = |\boldsymbol{r}|$. Also, let $\boldsymbol{u} = u_x\boldsymbol{e}_x + u_y\boldsymbol{e}_y + u_z\boldsymbol{e}_z$, p, and c represent, respectively, the *dimensionless*, steady-state velocity and pressure fields of the liquid and the concentration field of the chemical species. With these definitions and the conditions listed at the beginning of §2.2, the equations that govern the distributions of $\boldsymbol{u}$, p, and c in a coordinate system attached to the particle are (see, e.g., [72])

$$\begin{gathered}
\boldsymbol{\nabla}\cdot\boldsymbol{\sigma} - \mathrm{Re}\,(\boldsymbol{u} - \mathcal{U}\boldsymbol{e}_x)\cdot\boldsymbol{\nabla}\boldsymbol{u} = \nabla^2\boldsymbol{u} - \boldsymbol{\nabla}p - \mathrm{Re}\,(\boldsymbol{u} - \mathcal{U}\boldsymbol{e}_x)\cdot\boldsymbol{\nabla}\boldsymbol{u} = \boldsymbol{0} \quad \text{and} \quad \boldsymbol{\nabla}\cdot\boldsymbol{u} = 0, \\
\boldsymbol{u} = \mathcal{U}\boldsymbol{e}_x \text{ for } \boldsymbol{r} \in S_p, \qquad \boldsymbol{u} \to \boldsymbol{0} \text{ as } r \to \infty, \\
u_z = 0 \quad \text{and} \quad (\boldsymbol{I} - \boldsymbol{n}\boldsymbol{n})\cdot(\boldsymbol{n}\cdot\boldsymbol{\sigma}) = -\left(\frac{\partial u_x}{\partial z}\boldsymbol{e}_x + \frac{\partial u_y}{\partial z}\boldsymbol{e}_y\right) = -\boldsymbol{\nabla}_{2D}\gamma \text{ for } \boldsymbol{r} \in S_i
\end{gathered} \tag{2.10}$$

and

$$\nabla^2 c = \mathrm{Pe}\,(\boldsymbol{u} - \mathcal{U}\boldsymbol{e}_x)\cdot\boldsymbol{\nabla} c,$$

$$c \to 0 \text{ as } r \to \infty \qquad \text{and} \qquad \boldsymbol{n}\cdot\boldsymbol{\nabla} c = 0 \text{ for } \boldsymbol{r} \in S_i, \tag{2.11}$$

where

$$\mathrm{Re} = \frac{\rho U^\star \ell}{\mu}, \qquad \mathrm{Pe} = \frac{U^\star \ell}{\mathcal{D}}, \qquad \text{and} \qquad \mathcal{U} = \frac{U}{U^\star}, \tag{2.12}$$

with $\boldsymbol{U} = U\boldsymbol{e}_x$ being the propulsion velocity of the surfer and $U^\star$ denoting the value of U in the absence of advective effects (i.e, when $\mathrm{Re} = \mathrm{Pe} = 0$). Also, ℓ is the radius of the smallest sphere that encloses the geometry of the surfer.

Now, consider the auxiliary problem of Stokes flow around the same surfer travelling with velocity $\hat{\boldsymbol{U}} = \hat{U}\boldsymbol{e}_x$ (where $\hat{U} = |\hat{\boldsymbol{U}}|$) when no Marangoni effects are present. The (dimensionless) velocity and the stress fields in this case follow:

$$\boldsymbol{\nabla}\cdot\hat{\boldsymbol{\sigma}} = \nabla^2\hat{\boldsymbol{u}} - \boldsymbol{\nabla}\hat{p} = \boldsymbol{0} \quad \text{and} \quad \boldsymbol{\nabla}\cdot\hat{\boldsymbol{u}} = 0$$

$$\hat{\boldsymbol{u}} = \boldsymbol{e}_x \text{ for } \boldsymbol{r} \in S_p, \qquad \hat{\boldsymbol{u}} \to \boldsymbol{0} \text{ as } r \to \infty,$$

$$\hat{u}_z = 0 \quad \text{and} \quad (\boldsymbol{I} - \boldsymbol{nn})\cdot(\boldsymbol{n}\cdot\hat{\boldsymbol{\sigma}}) = -\left(\frac{\partial \hat{u}_x}{\partial z}\boldsymbol{e}_x + \frac{\partial \hat{u}_y}{\partial z}\boldsymbol{e}_y\right) = \boldsymbol{0} \text{ for } \boldsymbol{r} \in S_i. \tag{2.13}$$

Next, apply the reciprocal theorem between the velocity-stress pairs $(\boldsymbol{u}, \boldsymbol{\sigma})$ and $(\hat{\boldsymbol{u}}, \hat{\boldsymbol{\sigma}})$ (see, e.g., [72]):

$$\int_S \boldsymbol{n}\cdot\boldsymbol{\sigma}\cdot\hat{\boldsymbol{u}}\,\mathrm{d}S - \int_S \boldsymbol{n}\cdot\hat{\boldsymbol{\sigma}}\cdot\boldsymbol{u}\,\mathrm{d}S = \mathrm{Re}\int_V (\mathcal{U}\boldsymbol{e}_x - \boldsymbol{u})\cdot\boldsymbol{\nabla}\boldsymbol{u}\cdot\hat{\boldsymbol{u}}\,\mathrm{d}V. \tag{2.14}$$

Using integration by parts, incorporating the boundary conditions of Eqs. (2.10)-(2.13) and recognizing that the surface integrals at large distance vanish (since the velocities decay at least as fast as $1/r$), Eq. (2.14) simplifies to

$$\mathcal{U} = \frac{1}{\hat{F}} \left\{ - \int_{S_i} \gamma \, \boldsymbol{\nabla}_{2D} \cdot \hat{\boldsymbol{u}} \, \mathrm{d}S + \mathrm{Re} \left[\int_V \boldsymbol{u} \cdot \boldsymbol{\nabla} \hat{\boldsymbol{u}} \cdot \boldsymbol{u} \, \mathrm{d}V - \mathcal{U} \boldsymbol{e}_x \cdot \int_V \boldsymbol{\nabla} \hat{\boldsymbol{u}} \cdot \boldsymbol{u} \, \mathrm{d}V \right] \right\}, \tag{2.15}$$

where $\hat{F} = \int_{S_p} \boldsymbol{n} \cdot \hat{\boldsymbol{\sigma}} \, \mathrm{d}S$ is the dimensionless drag on the particle in the auxiliary problem. Equation (2.15) is an exact relation.

Suppose that $\mathrm{Re} \ll 1$ and $\mathrm{Pe} \ll 1$, and also assume that γ and c are linearly related as

$$\gamma = \gamma_0 - \frac{\alpha \, \dot{m}^\star}{2\pi \, \mathcal{D} \, \mu \, U^\star \, \ell} \, c, \tag{2.16}$$

where γ and c are made dimensionless by $\mu \, U^\star$ and $\dot{m}^\star / 2\pi \, \mathcal{D} \, \ell$, respectively, with $\dot{m}^\star$ being the release rate of the chemical species when $\mathrm{Pe} = 0$. In the limits of small Re and Pe, the velocity and concentration fields can be expressed in the form of the following uniformly valid expansions:

$$\begin{aligned} \boldsymbol{u} = {} & \boldsymbol{u}^{(0,0)} + \mathrm{Re} \ln \mathrm{Re} \, \boldsymbol{u}^{(1,0)} + \mathrm{Re} \, \boldsymbol{u}^{(2,0)} \\ & + \left(\mathrm{Re} \, \underset{\sim}{\boldsymbol{u}}^{(1,0)} - \boldsymbol{u}_\infty^{(0,0)} - \mathrm{Re} \ln \mathrm{Re} \, \boldsymbol{u}_\infty^{(1,0)} - \mathrm{Re} \, \boldsymbol{u}_\infty^{(2,0)} \right) + \mathcal{O}(\mathrm{Re}^2 \ln \mathrm{Re}) + \mathcal{O}(\mathrm{Pe} \ln \mathrm{Pe}), \end{aligned} \tag{2.17}$$

$$c = c^{(0,0)} + \mathrm{Pe} \, c^{(0,1)} + \left(\mathrm{Pe} \, \underset{\sim}{c}^{(0,1)} - c_\infty^{(0,0)} - \mathrm{Pe} \, c_\infty^{(0,1)} \right) + \mathcal{O}(\mathrm{Pe}^2 \ln \mathrm{Pe}) + \mathcal{O}(\mathrm{Pe} \, \mathrm{Re} \ln \mathrm{Re}), \tag{2.18}$$

where the infinity subscript denotes the leading-order contributions to the corresponding terms in the limit that $r \to \infty$. It can be shown that

$$\hat{\boldsymbol{u}} = \frac{1}{4\pi r}\left(\boldsymbol{I} + \frac{\boldsymbol{r}\boldsymbol{r}}{r^2}\right) \cdot \hat{F}\,\boldsymbol{e}_x + \mathcal{O}(r^{-2}), \tag{2.19}$$

$$\boldsymbol{u}^{(0,0)} = \left(\frac{\alpha\,\dot{m}^\star}{4\pi\,\mathcal{D}\,\mu\,U^\star\,\ell}\right)\frac{1}{r}\left[(1+2\cos\theta)\,\boldsymbol{e}_r + \frac{\sin\theta\cos\theta}{1-\cos\theta}\boldsymbol{e}_\theta\right] + \mathcal{O}(r^{-2}), \tag{2.20}$$

$$\begin{aligned}\underset{\sim}{\boldsymbol{u}}^{(1,0)} = -\left(\frac{\alpha\,\dot{m}^\star}{\mathcal{D}\,\mu\,U^\star\,\ell}\right)\mathfrak{F}_{2D}^{-1}\Bigg\{\frac{i\underset{\sim}{\boldsymbol{k}}}{\boldsymbol{e}_x\cdot i\underset{\sim}{\boldsymbol{k}}}\Bigg\{&\exp(\underset{\sim}{k}z) - \exp\left(\sqrt{\underset{\sim}{k}^2 - \boldsymbol{e}_x\cdot i\underset{\sim}{\boldsymbol{k}}}\,\underset{\sim}{z}\right)\\ &- \left(\sqrt{1 - \frac{\boldsymbol{e}_x\cdot i\underset{\sim}{\boldsymbol{k}}}{\underset{\sim}{k}^2}} - 1\right)\exp\left(\sqrt{\underset{\sim}{k}^2 - \boldsymbol{e}_x\cdot i\underset{\sim}{\boldsymbol{k}}}\,\underset{\sim}{z}\right)\\ &+ \frac{\underset{\sim}{k}\,\boldsymbol{e}_z}{i\underset{\sim}{\boldsymbol{k}}}\left[\exp(\underset{\sim}{k}z) - \exp\left(\sqrt{\underset{\sim}{k}^2 - \boldsymbol{e}_x\cdot i\underset{\sim}{\boldsymbol{k}}}\,\underset{\sim}{z}\right)\right]\Bigg\}\Bigg\},\end{aligned} \tag{2.21}$$

$$c^{(0,0)} = \frac{1}{r} + \mathcal{O}(r^{-2}), \tag{2.22}$$

$$c^{(0,1)} = -\frac{1}{2}\left(1 + \frac{x}{r}\right) + \mathcal{O}(r^{-1}), \tag{2.23}$$

$$\underset{\approx}{c}^{(0,1)} = \frac{1}{\underset{\sim}{r}}\exp\left[-\frac{1}{2}\left(\underset{\sim}{r} + \underset{\approx}{x}\right)\right] = \frac{1}{\underset{\sim}{r}} - \frac{1}{2}\left(1 + \frac{\underset{\approx}{x}}{\underset{\sim}{r}}\right) + \mathcal{O}(\underset{\sim}{r}), \tag{2.24}$$

where $\sim$ and $\approx$ underbars denote that the velocity and concentration fields as well as the $\boldsymbol{\nabla}$ operator are written in terms of the stretched (rescaled) position vectors $\underset{\sim}{\boldsymbol{r}} = \mathrm{Re}\,\boldsymbol{r}$ and $\underset{\approx}{\boldsymbol{r}} = \mathrm{Pe}\,\boldsymbol{r}$, respectively. Substituting the above equations into Eq. (2.15), we arrive at

$$\mathcal{U} = 1 - \frac{\alpha\,\dot{m}^\star}{32\pi\,\mathcal{D}\,\mu\,U^\star\,\ell}\left(\mathrm{Re}\ln\mathrm{Re} + 2\,\mathrm{Pe}\ln\mathrm{Pe}\right) + \mathcal{O}(\mathrm{Re}) + \mathcal{O}(\mathrm{Pe}). \tag{2.25}$$

Equation (2.25) reveals a very important point: that the propulsion speed increases with increasing Re and Pe from zero when α is positive. We will expand on this finding in chapter §4, where we numerically compute U for a wide ranges of Re and

Pe.

As a special case, consider a surfer whose wetted surface is divided into active S_p^a and inactive S_p^{ia} segments with, respectively, uniform concentration c_s and zero mass flux ($\boldsymbol{n} \cdot \boldsymbol{\nabla} c = 0$) prescribed on them. It can be shown that, in this case, the total release rate of the chemical species can be expressed as

$$\mathrm{Sh} = \mathrm{Sh}^\star + \frac{(\mathrm{Sh}^\star)^2}{2}\mathrm{Pe} + \mathcal{O}(\mathrm{Pe}^2 \ln \mathrm{Pe}) + \mathcal{O}(\mathrm{Pe}\,\mathrm{Re} \ln \mathrm{Re}) \tag{2.26}$$

where

$$\mathrm{Sh} = \frac{\dot{m}}{2\pi\,\mathcal{D}\,\ell\,c_s} \quad \text{and} \quad \mathrm{Sh}^\star = \frac{\dot{m}^\star}{2\pi\,\mathcal{D}\,\ell\,c_s}. \tag{2.27}$$

Chapter 3: A Computational Framework for Simulating Marangoni Surfing

3.1 Introduction

Deriving exact or even approximate formulas for the Marangoni propulsion at moderate and high Reynolds and Péclet numbers is challenging, if not impossible. Therefore, we resort to numerics to study the Marangoni-driven motion of active particles when the inertial effects and flow-driven transport of the chemical species are no longer negligible. Detailed numerical solutions allow us to visualize the flow and concentration fields around the surfer, in addition to obtaining its propulsion speed. This then enables us to develop a deeper understanding of Marangoni propulsion. Also, numerical simulations are generally more accommodating when it comes to including additional complexities, which means that they can be used to examine the propulsion behavior of active surfers under various complicated conditions. In this chapter, we introduce a high-fidelity computational framework for simulating Marangoni surfing. The details of our approach is described in the following sections.

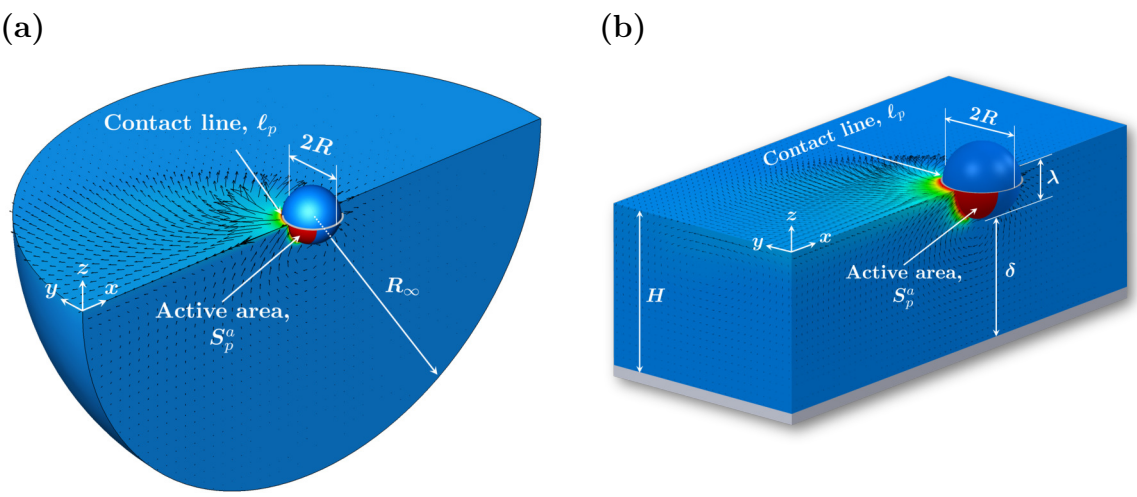

Figure 3.1: Schematics of a half-submerged spherical surfer located atop (a) (ideally) unbounded and (b) confined liquid layers. The active area of the surfer that is colored red shows the release area. The color map and vector plots represent the concentration distribution and liquid velocity field in the vicinity of the surfer, respectively.

3.2 Governing Equations

For the purposes of our simulations, we assume that the movement of the surfer is caused by the release of a chemical species from the active region of its surface, on which the concentration of the chemical species c is constant (see Fig. 3.1). Denoted by S_p^a, this area mimics a realistic scenario where the surfer is dip-coated on one side to a depth of d by a layer of active agent such as alcohol (see [81] and §4.4.1). Hence, applying assumptions similar to those outlined in chapter §2, the equations

that govern the spatio-temporal evolution of $\boldsymbol{u}$, p, and c can be expressed as

$$\begin{aligned}
&\rho\left(\frac{\partial \boldsymbol{u}}{\partial t}+\boldsymbol{u}\cdot\boldsymbol{\nabla}\boldsymbol{u}\right)=-\boldsymbol{\nabla}p+\mu\nabla^2\boldsymbol{u} \quad \text{and} \quad \boldsymbol{\nabla}\cdot\boldsymbol{u}=0, \quad \text{with} \\
&\boldsymbol{u}\left(\boldsymbol{r},0\right)=\boldsymbol{0}, \quad \boldsymbol{u}=\boldsymbol{U} \text{ for } \boldsymbol{r}\in S_p, \quad \boldsymbol{u}=\boldsymbol{0} \text{ for } \boldsymbol{r}\in S_w, \\
&u_z=0 \quad \text{and} \quad (\boldsymbol{I}-\boldsymbol{nn})\cdot(\boldsymbol{n}\cdot\boldsymbol{\sigma})=-\mu\left(\frac{\partial u_x}{\partial z}\boldsymbol{e}_x+\frac{\partial u_y}{\partial z}\boldsymbol{e}_y\right)= \\
&-\boldsymbol{\nabla}_s\gamma=-\left(\frac{\partial \gamma}{\partial x}\boldsymbol{e}_x+\frac{\partial \gamma}{\partial y}\boldsymbol{e}_y\right) \quad \text{for } \boldsymbol{r}\in S_i,
\end{aligned} \tag{3.1}$$

$$\begin{aligned}
&\frac{\partial c}{\partial t}+\boldsymbol{u}\cdot\boldsymbol{\nabla}\boldsymbol{c}=\mathcal{D}\nabla^2\boldsymbol{c}, \quad \text{with} \\
&c\left(\boldsymbol{r},0\right)=0, \quad c=c_s \text{ for } \boldsymbol{r}\in S_p^a, \quad \boldsymbol{n}\cdot\boldsymbol{\nabla}c=0 \text{ for } \boldsymbol{r}\notin S_p^a,
\end{aligned} \tag{3.2}$$

where

$$\boldsymbol{\sigma}=-p\boldsymbol{I}+\mu\left[\boldsymbol{\nabla}\boldsymbol{u}+(\boldsymbol{\nabla}\boldsymbol{u})^T\right], \tag{3.3}$$

$$\gamma=\gamma_0-\alpha\, c. \tag{3.4}$$

Here, S_p, S_w, S_i, $\boldsymbol{\sigma}$, $\boldsymbol{I}$, and $\boldsymbol{n}$ denote the wetted surface of the surfer, the bounding walls, the liquid-gas interface, the stress tensor, the identity tensor, and the unit normal vector, respectively. And, c_s, γ_0, and α are positive constant parameters. The instantaneous linear and angular velocities of the surfer ($\boldsymbol{U}=U_x\,\boldsymbol{e}_x+U_y\,\boldsymbol{e}_y$ and $\boldsymbol{\omega}=\omega\,\boldsymbol{e}_z$, respectively) are determined via

$$\int_{\ell_p}\gamma\boldsymbol{t}\,\mathrm{d}\ell+\int_{S_p}\boldsymbol{n}\cdot\boldsymbol{\sigma}\,\mathrm{d}S=m\,\frac{d\boldsymbol{U}}{dt} \quad \text{with} \quad \boldsymbol{U}(t=0)=\boldsymbol{0}, \tag{3.5}$$

$$\int_{\ell_p}\boldsymbol{r}\times\gamma\boldsymbol{t}\,\mathrm{d}\ell+\int_{S_p}\boldsymbol{r}\times\boldsymbol{n}\cdot\boldsymbol{\sigma}\,\mathrm{d}S=\boldsymbol{I}_{zz}\,\frac{d\omega}{dt}\,\boldsymbol{e}_z \quad \text{with} \quad \omega(t=0)=0, \tag{3.6}$$

where the sum of the integrals on the left-hand sides of Eqs. (3.5) and (3.6) represent, respectively, the total force and moment experienced by the surface (ignoring the load exerted by the gas phase). Here, ℓ_p denotes the three-phase contact line, $\boldsymbol{t}$ is the unit vector tangent to S_i and normal to ℓ_p, m is the mass of the surfer and I_{zz} is its moment of inertia about the z axis. Note that all quantities in the above equations are dimensional.

3.3 Numerical Scheme

To solve the aforementioned governing equations numerically, we use a second-order finite-volume method as implemented in *OpenFOAM* (see, e.g., [82]). In our numerical calculations, the Laplacians and gradients are discretized via the second-order linear Gaussian integration, the corrected scheme (with the number of corrections set to one or two depending on the non-orthogonality of the mesh) is used to calculate surface normal gradients, the time derivatives are approximated by the second-order backward differentiation formula, and the equation of motion for the surfer is integrated using the Newmark method with the relaxation parameter set to 0.5. The PIMPLE algorithm is employed to treat the pressure-velocity coupling and the linear solver GAMG (Geometric-Algebraic Multi-Grid) with DIC (Diagonal Incomplete-Cholesky) preconditioner is used to solve for the pressure. Finally, the Gauss-Seidel method is utilized to calculate the velocity and concentration fields.

3.4 Surfer's Kinematics

Depending on the problem under consideration, we use two different ways to capture the motion of the surfer and to couple its movement with the flow of the surrounding fluid and the transport of the released agents. The approaches are detailed below.

3.4.1 Non-Inertial Reference Frame

When the surfer's motion is restricted to pure translation, we rewrite the coupled initial-boundary-value problem described by the Navier-Stokes equations (3.1), the advection-diffusion equation (3.2), and Newton's equation of motion (3.5) in a non-inertial reference frame attached to the surfer (see, e.g., [83]). The process involves substituting $\boldsymbol{u}$ with $\boldsymbol{v} = \boldsymbol{u} - \boldsymbol{U}$ in Eqs. (3.1) and (3.2) and adding a source term equal to $-\rho\, d\boldsymbol{U}/dt$ to the right-hand side of the momentum balance expression in Eq. (3.1). Also, we set the fluid velocity on S_p to zero and apply the negative of the instantaneous propulsion velocity of the surfer, that is calculated from Eq. (3.5), to the stationary outer boundaries (see also §3.5). Using this approach, we avoid dealing with a moving boundary (and, hence, a moving mesh) problem. Moreover, we make sure that the surfer is always far enough from the external boundaries that model the far-field conditions.

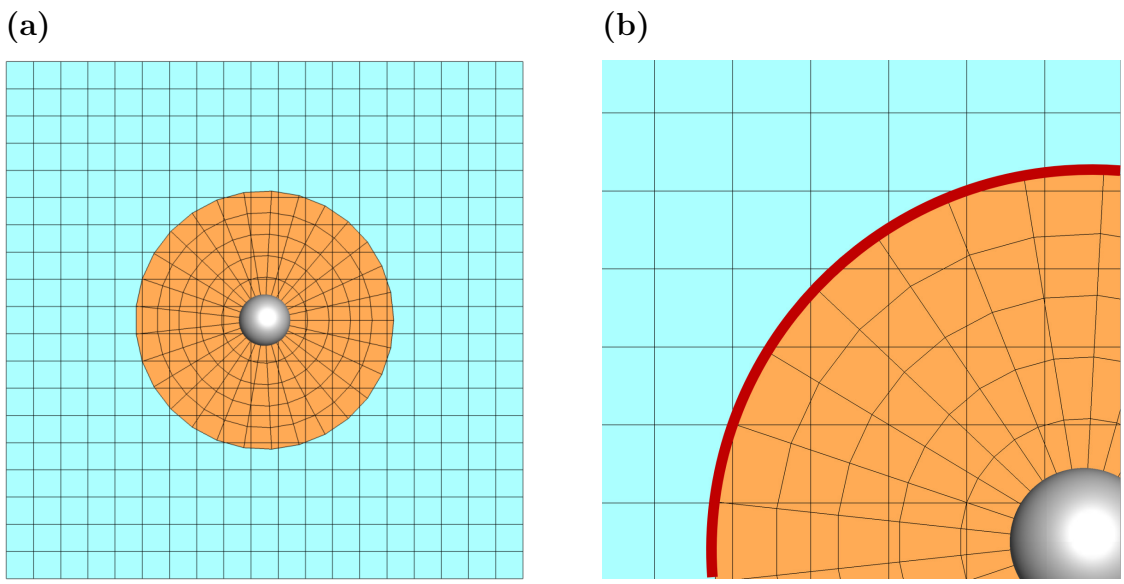

Figure 3.2: A simple example of overset gridding.

3.4.2 Overset Grid

In cases where the surfer both translates and rotates, we adopt a moving mesh approach to simulate the surfer's kinematics. Specifically, we employ overset grids [84–90] to handle the moving boundary problem resulting from the motion of the surfer. In the overset-grid method (which is also known as chimera [91, 92] and overlapping-grid method [93–95]) the computational domain is decomposed into multiple overlapping grids. The governing equations are separately solved for each grid and the connection between different sub-domains is achieved through interpolating over the overlapping zones [96]. Figure 3.2 shows a simple example of overset gridding, where a rectangular domain with a circular inclusion is discretized via two overlapping meshes. The first sub-domain is a simple Cartesian grid (the blue zone) that conforms to the outer

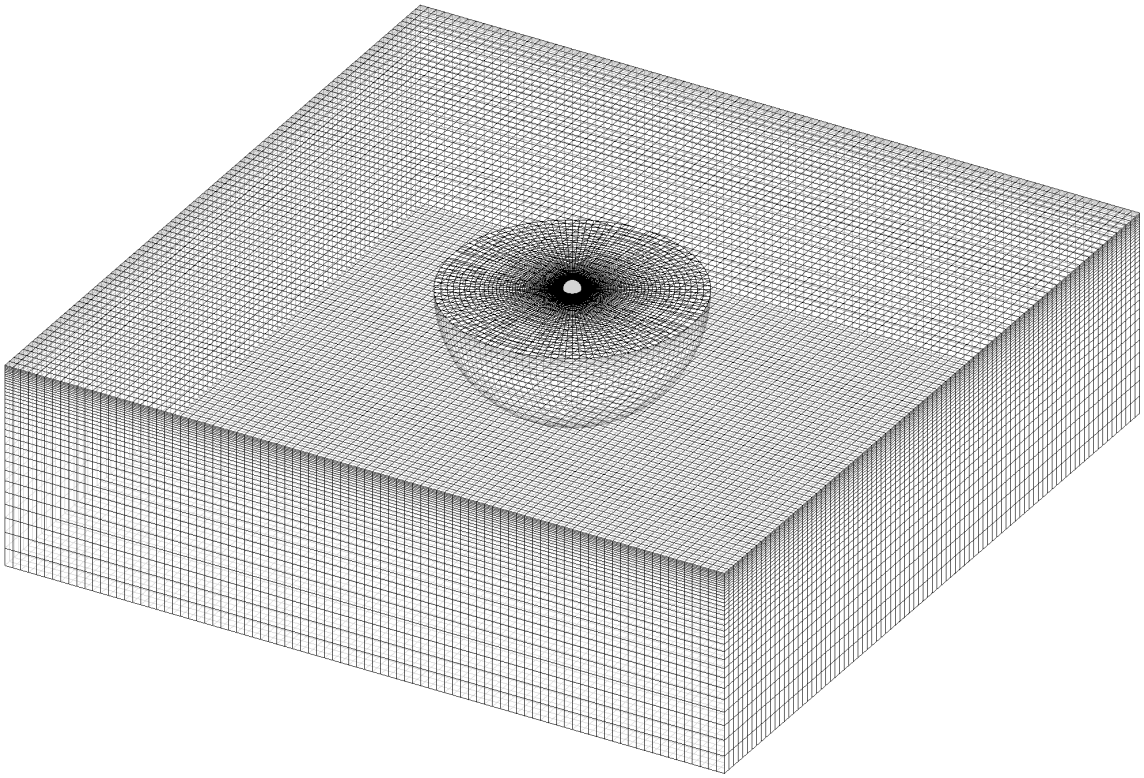

Figure 3.3: An example of the overset mesh used to simulate the surfing motion of a sphere.

boundaries and the other sub-domain is a boundary-fitted grid around the object (the orange zone). The governing equations are treated separately over each zone and an interpolation in the neighbourhood of the red line in Fig. 3.2b establishes the connectivity of the domains.

To implement overset gridding in our simulations, we use two overlapping grids: a background Cartesian mesh and one that fits the boundary of the surfer and extends $15R$ (where R is the characteristic length of the surfer) into the liquid (see, e.g., Fig. 3.3). The former is stationary whereas the latter moves with the surfer. As before, when the goal is to simulate the motion of the surfer along an unbounded liquid-gas interface, we express the governing equations in a reference frame that translate

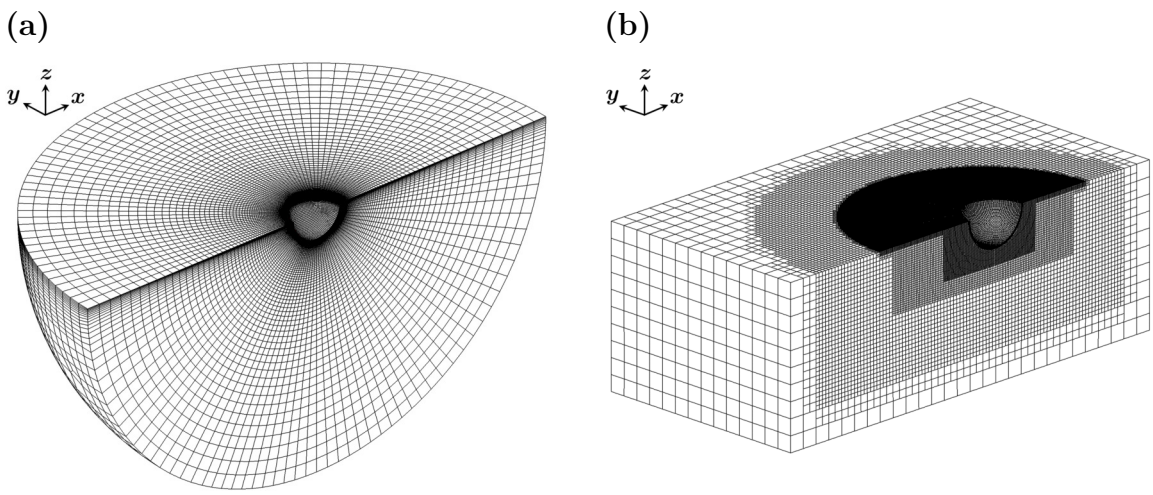

Figure 3.4: Portions of sample computational domains corresponding to (a) (ideally) unbounded and (b) confined liquid layers.

with the surfer. This allows us to avoid unwanted boundary effects. Lastly, we use the inverse distance weighting method to carry out the interpolations over the overlapping zone, and make sure that the mesh sizes are comparable in this region.

3.5 Computational Domain and Boundaries

In the absence of a confining wall, we set the computational domain to a very large hemisphere with the submerged volume of the surfer carved out of its top center (see Fig. 3.1a). This configuration allows for the use of the sweeping meshing technique to discretize the domain. Via this method, we are able to achieve a high-quality mesh that is concentrated near the surfer and close to the interface, where large gradients are expected to reside (see Fig. 3.4a). The radius of the hemisphere is generally chosen to be $100R$. However, when the effect of the outer boundary becomes more significant

(i.e., when Re $\lesssim 0.01$ or Pe $\lesssim 0.01$), the radius is made 10 times larger to more closely model an unconfined domain. Note that, for clarity, Fig. 3.4a shows only portions of the computational domains.

To simulate Marangoni propulsion when there exists a confining solid wall below the interface, we set the computational domain to a rectangular box of length L, width W, and height H (see Fig. 3.1b). The domain is then discretized using the *snappyHexMesh* utility of *OpenFOAM* in a multi-block fashion, where the mesh is densely distributed near the surfer. When the simulations are intended for comparison with the experiments, the size of the domain and the depth of the surfer's active region are matched with the experimental values (see §4.4.1). Otherwise, we set $L = 100R$, $W = 50R$, and $d = R/2$, and vary H to adjust the degree of confinement.

As indicated in the previous section, the computational domain is also set to a rectangular box with $L = W = 2H = 50R$ when using overset-grid method. In that case, the conforming mesh attached to the surfer is considered to be a hemisphere of radius $15R$ with the geometry of the surfer curved out of its top center.

3.6 Validation Studies

The following validation studies are performed to confirm the fidelity and robustness of the computational approach outlined in this chapter.

3.6.1 Comparison with Theory and Experiment

We begin by comparing the results of our simulations for the propulsion speed with the theoretical predictions of the previous chapter. The comparisons are made for a spherical surfer with radius R and $d = R/2,\ R,\ 3R/2$ at $\mathrm{Re} = 0.01, 0.1$ and $\mathrm{Pe} = 0.01, 0.1$. Table 3.1 shows the percent difference between the theoretically predicted and numerically calculated values for the normalized speed. We see a very good agreement between the theoretical and numerical results, which not only demonstrates the validity of the simulations, but also is indicative of the accuracy of the theoretical predictions. Next, we compare the results of our simulations against a set of experimental data for Marangoni propulsion under confinement. To avoid duplicate descriptions, the details

d	Re	0.01	0.10	0.01	0.10
	Pe	0.01	0.01	0.10	0.10
$\frac{R}{2}$	Simulation	1.104938	1.293394	1.434654	1.607442
	Theory	1.134524	1.313470	1.492417	1.671363
	Difference (%)	2.677602	1.552239	4.026206	3.976624
R	Simulation	1.194949	1.582321	1.830097	2.164345
	Theory	1.234127	1.546297	1.858466	2.170636
	Difference (%)	3.278601	2.276691	1.550128	0.290640
$\frac{3R}{2}$	Simulation	1.487038	2.594449	2.894312	3.857013
	Theory	1.541421	2.263316	2.985210	3.707105
	Difference (%)	3.657115	12.76314	3.140582	3.886638

Table 3.1: Comparison between the numerically calculated and theoretically obtained results for the normalized propulsion speed $\mathcal{U}$.

of the comparison are presented later in §4.4.1 of the next chapter, where we discuss the effects of the thickness of the liquid layer on the Marangoni propulsion. But, in short, we observe excellent corroboration between simulated and measured data (see Figs. 4.13 and 4.14).

3.6.2 Grid Independence Tests

Throughout our study, we have conducted many tests to ensure that the results of the simulations are not dependent on a particular choice of mesh. For brevity, here, we only report illustrative tests performed for the extreme cases of Pe = 1000 and Re = $0.01, 1000$. To verify that the results are grid-independent, the results of four different meshes for the normalized propulsion speed are compared against each other. The comparisons are made for a spherical surfer with $d = R/2$ that propels on top of a

	Mesh 1	Mesh 2	Mesh 3	Mesh 4
Δx_s^{max}	0.05	0.05	0.05	0.025
N_i	7	14	14	19
G_i	1.26	1.19	1.19	1.15
N_r	120	120	200	120
G_r	1.060	1.060	1.032	1.078
Total mesh	$203,760$	$259,200$	$434,200$	$569,880$
$\mathcal{U}$ at Re = 0.01	1.032	0.790	0.769	0.787
$\mathcal{U}$ at Re = 1000	0.244	0.250	0.251	0.250

Table 3.2: Specifications of the meshes used in the grid-independence study.

semi-infinite liquid layer. Table 3.2 shows the specifications of each mesh, where Δx_s^{max} is the maximum mesh size on the surface of the surfer, N_i and G_i are, respectively, the number of grids and the grid growth rate across the estimated concentration boundary layer underneath the interface, and N_r and G_r are, respectively, the total number of grids and the grid growth rate in the radial direction. We see that, overall, the results obtained from different mesh configurations are similar. We also observe that it is important to fully resolve the concentration gradients near the interface, particularly when Pe is large and Re is small.

Chapter 4: Optimal, Stable, and Reverse Marangoni Propulsion

4.1 Introduction

Building on the knowledge gain from the theoretical results of chapter §2, in this chapter, we numerically examine three aspects of the Marangoni propulsion using the approach described in chapter §3. First, we consider the variations of the speed as a function of Re and Pe in the absence of a confining solid boundary. Then, we analyze the stability of the Marangoni surfing under the same conditions. Finally, we investigate the propulsion behavior of the surfers when the liquid layer is bounded from below by a solid wall. Details of the examinations are discussed in the following sections.

4.2 Optimal Marangoni Propulsion

We have learned from Eq. (2.25) that, when the Reynolds and Péclet numbers are small (i.e., $\mathrm{Re} \ll 1$ and $\mathrm{Pe} \ll 1$), the propulsion speed benefits from stronger advective effects. A natural question that follows this discovery is that whether the trend continues as Re and Pe become larger, reaching $\mathcal{O}(1)$ and increasing even further until they

are both much greater than one. Also, perhaps as important as the speed, is the efficiency of the propulsion. Therefore, it is critical to know how the efficiency varies with increasing Re and Pe, too. To address these inquiries, we simulate the surfing motion of a spherical surfer with $d = R/2$, R, $3R/2$ at Re = 0.01, 0.1, 1, 10, 100, 1000 and Pe = 0.01, 0.1, 1, 10, 100, 1000. Note that these Reynolds and Péclet numbers are nominal values defined the same way as in chapter §2 (see Eq. (2.12)). Therefore, the actual (or effective) values of Re and Pe may differ from the nominal ones depending on the magnitude of the actual propulsion speed determined by the simulations.

Figures 4.1, 4.2, and 4.3 illustrate the outcome of the simulations for $d = R/2$, R, and $3R/2$, respectively. The results are presented in the form of contour plots of normalized propulsion speed $\mathcal{U}$ and fuel efficiency $\mathcal{E}$ versus Re and Pe, where the latter is defined as

$$\mathcal{E} = \frac{U/\mathrm{Sh}}{U^\star/\mathrm{Sh}^\star} = \frac{\mathcal{U}}{\mathrm{Sh}/\mathrm{Sh}^\star}. \tag{4.1}$$

with $\mathrm{Sh}^\star$ representing the total (dimensionless) release rate (i.e., fuel consumption) corresponding to Pe = 0 (see Eq. (2.27)). Interestingly, we see that, in all cases, both $\mathcal{U}$ and $\mathcal{E}$ initially rise with increasing Re and Pe from zero, then reach a maximum, and eventually decline as advective (momentum/mass) transport dominates diffusion. This indicates that for each surfer there exist $(\mathrm{Re}, \mathrm{Pe})$ pairs at which $\mathcal{U}$ and $\mathcal{E}$ peak. While the maximums do not occur at the same $(\mathrm{Re}, \mathrm{Pe})$ pair, they take place approximately when $\mathrm{Re} \sim \mathrm{Pe} \sim \mathcal{O}(1)$.

To gain additional insights into the propulsion behavior of the surfers, we also

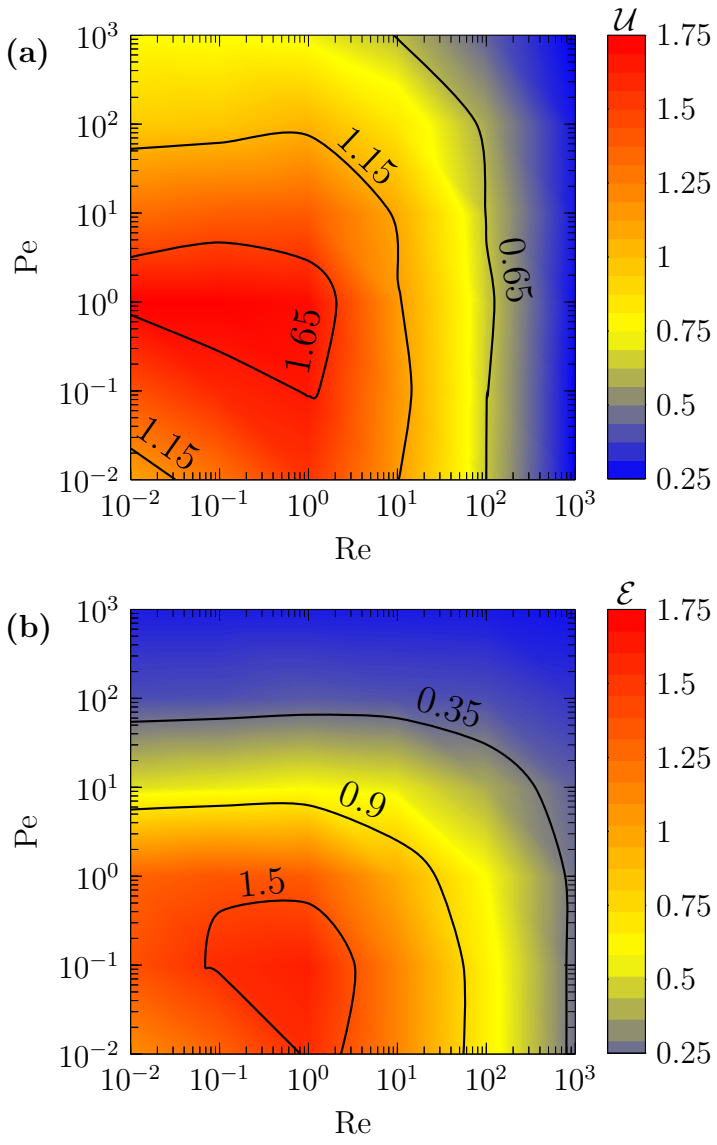

Figure 4.1: Contour plots of normalized (a) propulsion speed and (b) fuel efficiency for a spherical surfer with $d = R/2$.

examine the fluid flow and concentration distribution around them. To avoid duplicity, we only consider cases with Pe = 0.1, 10, 1000, Re = 1, 100, and $d = R/2$ (see Figs. 4.4, 4.5, 4.6, and 4.7). As expected, we see that the discharge of the active agent leads to the propulsion of the surfer and also causes the interface to dilate somewhat radially from a stagnation point adjacent to the release site. This point coincides with

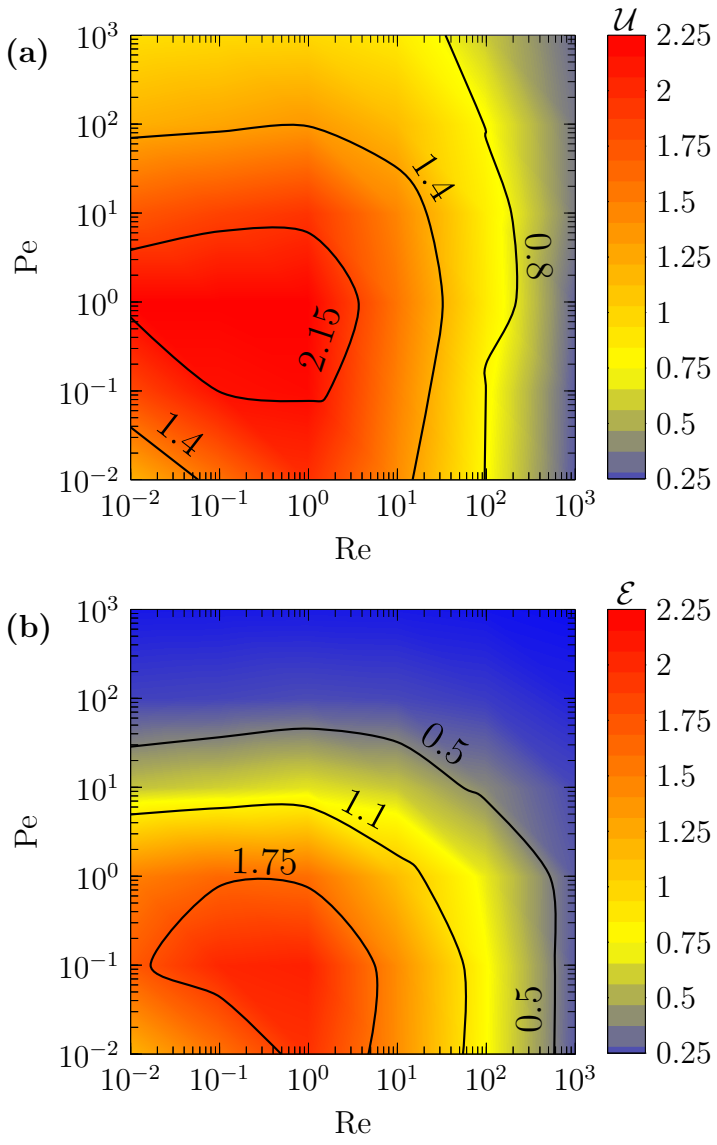

Figure 4.2: Contour plots of normalized (a) propulsion speed and (b) fuel efficiency for a spherical surfer with $d = R$.

the location of minimum interfacial tension (see Figs. 4.4d and 4.5d). The motion of the surfer combined with the diverging interfacial flow due to the dilation gives rise to a flow pattern underneath the free surface that resembles a deformed vortex ring. The vortex originates from the reversed flow in the bulk that is necessary to maintain the conservation of mass (i.e. a divergence-free flow). When projected onto the x-z

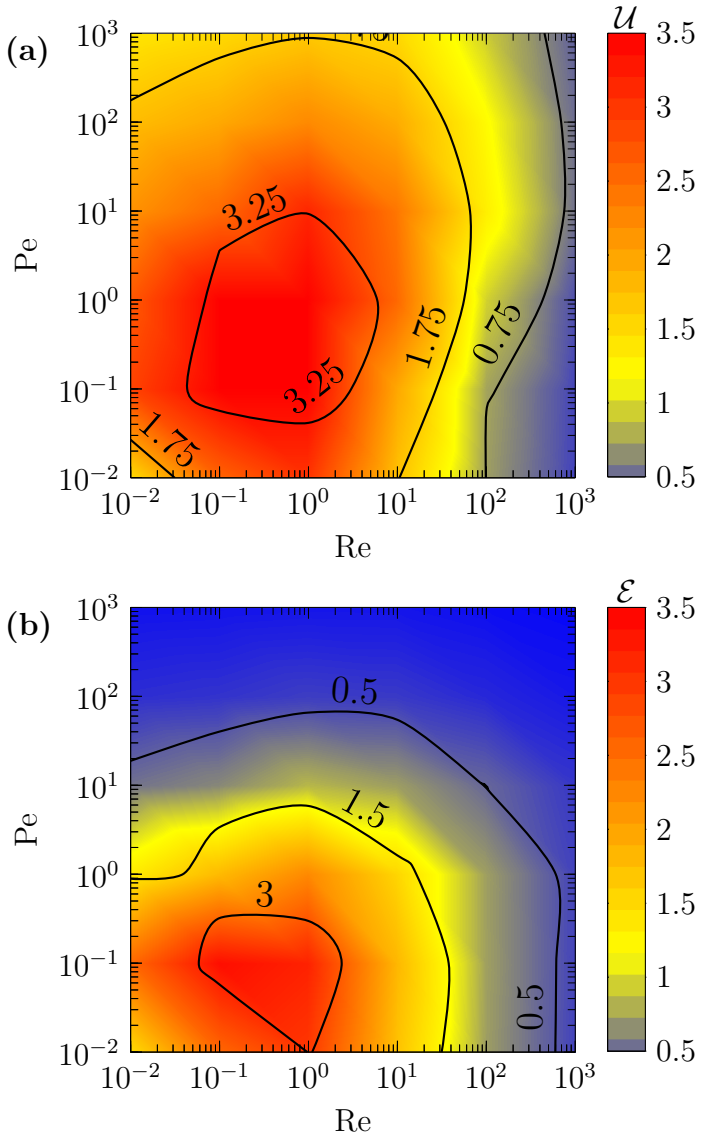

Figure 4.3: Contour plots of normalized (a) propulsion speed and (b) fuel efficiency for a spherical surfer with $d = 3R/2$.

plane bisecting the surfer, the three-dimensional swirling flow appears as a pair of counter-rotating vortices, one below the surfer and the other one to the left of the stagnation point (see figures 4.4b and 4.5b). This pattern is the main characteristics of the flow around a Marangoni surfer that distinguishes it from the flow created by the motion of an otherwise inert particle at the interface (see Figs. 4.4d and 4.5d and

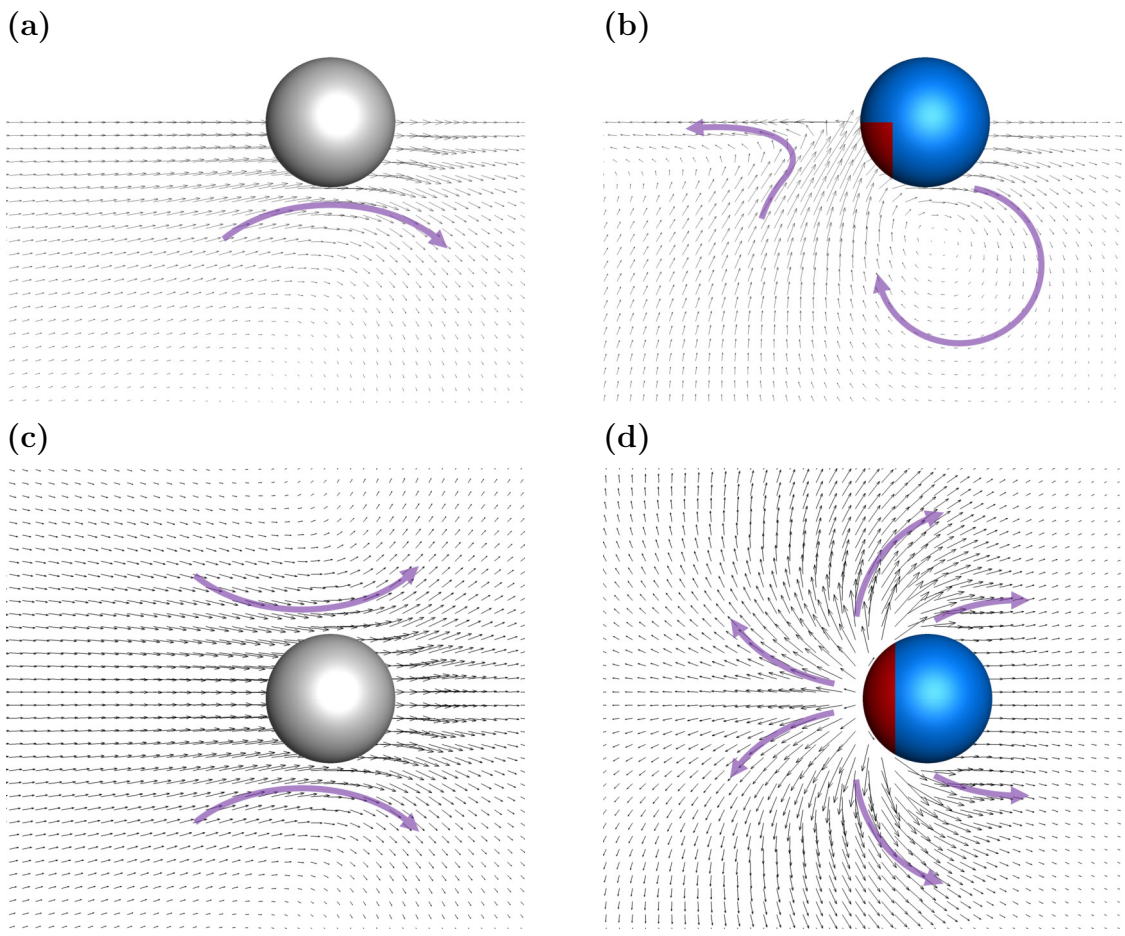

Figure 4.4: Flow field plots corresponding to a Translating spheroidal surfer with no Marangoni at the interface and (left panel) and Marangoni-driven motion of an active sphere at Pe = 10 (right panel) at Re = 1. The top row shows the fluid flow in the x-z plane bisecting the surfer, and the bottom row illustrates the velocity field at the water-air interface. The purple thick arrows highlight the direction of the flow. The black arrows in the vector field are scaled independently in each panel to facilitate flow visualization. The direction of propulsion is from left to right.

compare them with Figs. 4.4c and 4.5c). For instance, Fig. 4.4a clearly shows that, at low Re, no vortex is formed underneath the free surface or below the inactive particle. Finally, contrasting Figs. 4.6 and 4.7, we also observe that the general form of the flow structure in the vicinity of the surfer is similar for different Péclet numbers. However,

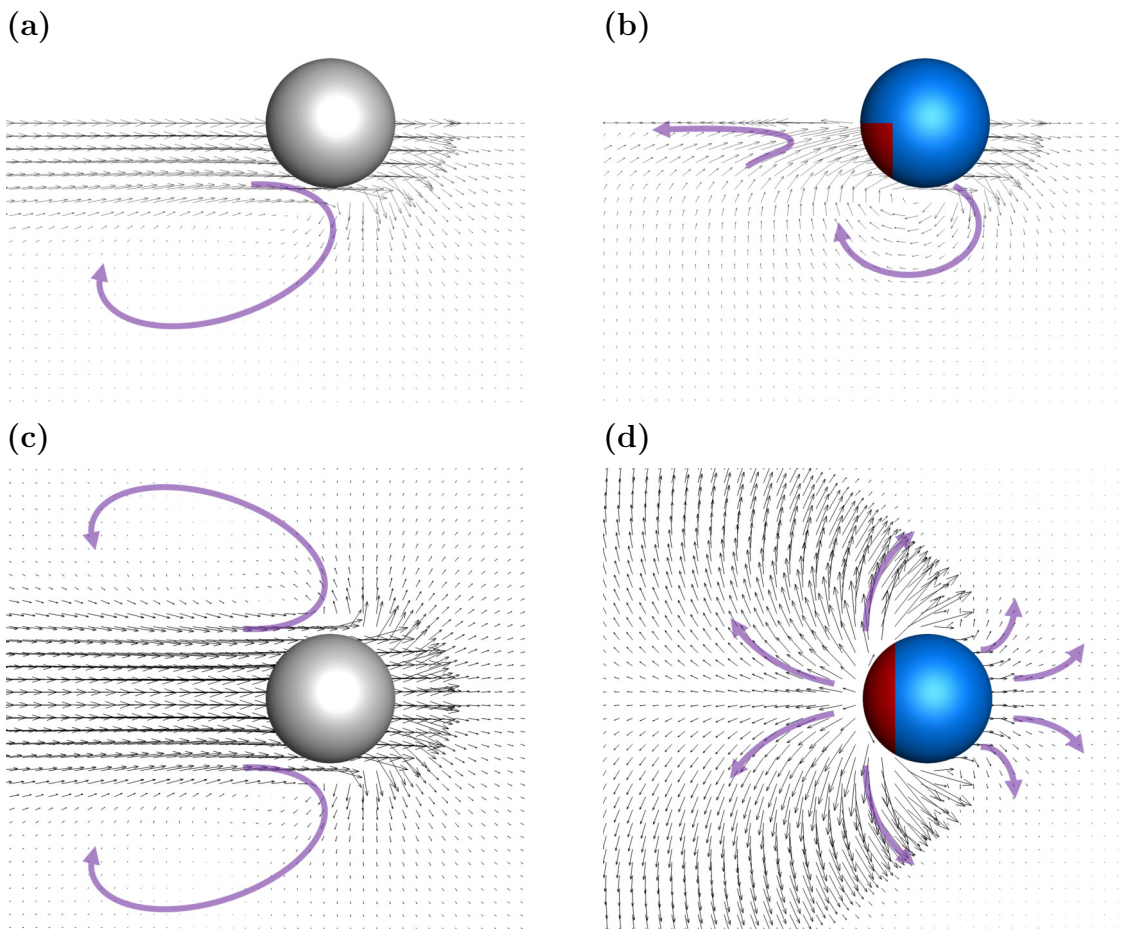

Figure 4.5: Flow field plots corresponding to a Translating spheroidal surfer with no Marangoni at the interface and (left panel) and Marangoni-driven motion of an active sphere at Pe = 10 (right panel) at Re = 100. The top row shows the fluid flow in the x-z plane bisecting the surfer, and the bottom row illustrates the velocity field at the water-air interface. The purple thick arrows highlight the direction of the flow. The black arrows in the vector field are scaled independently in each panel to facilitate flow visualization. The direction of propulsion is from left to right

there exist subtle difference, particularly when the Reynolds number is high (see, e.g., Figs. 4.6b and 4.6d).

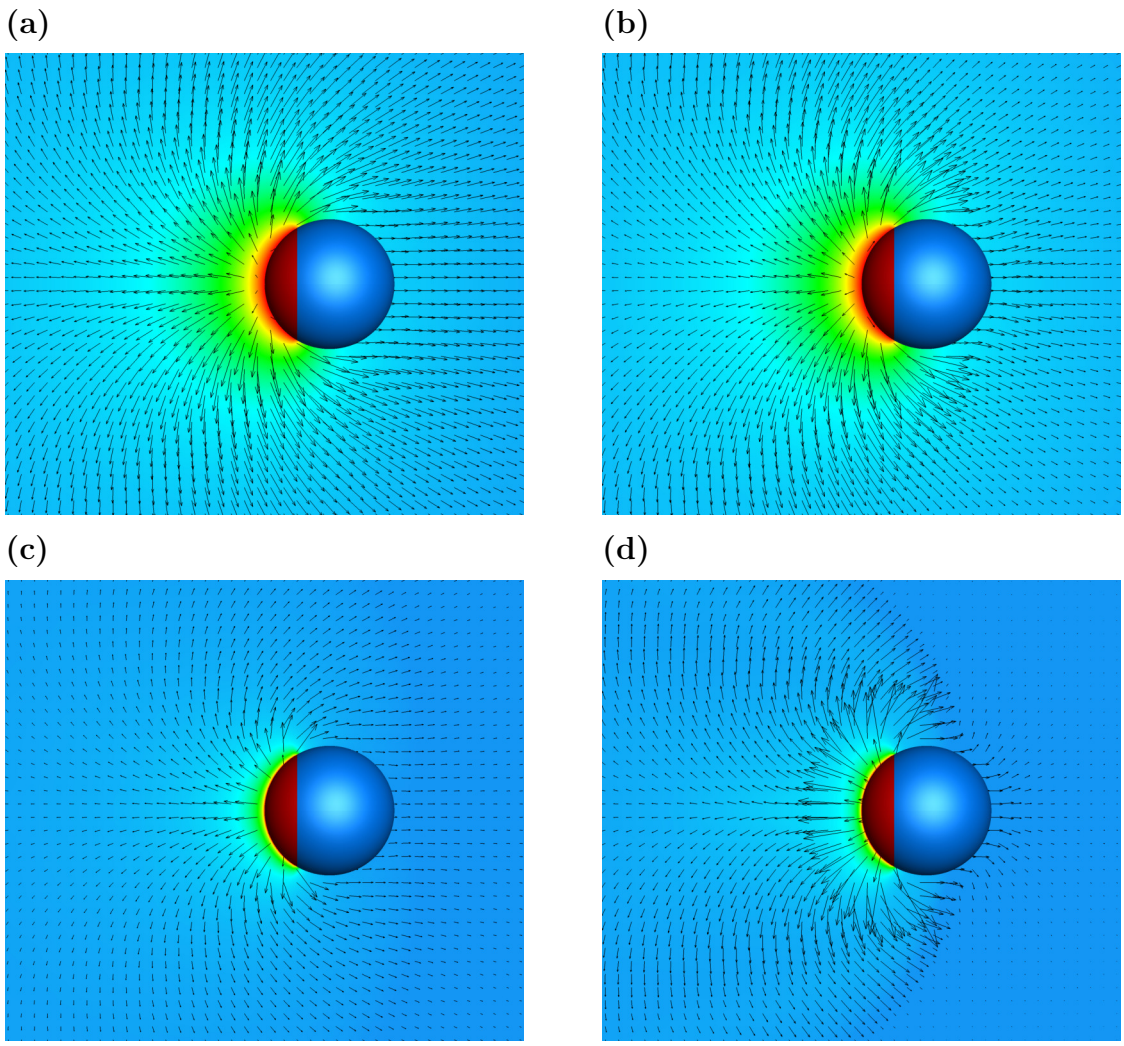

Figure 4.6: Velocity field and contour of active chemical concentration at the interface corresponding to the Marangoni-driven motion of an active sphere at Re = 1 (left panel) and Re = 100 (right panel). The top and bottom rows show, respectively, the result at Pe = 0.1 and Pe = 1000. In the color maps the concentration is the highest at the active area of the surfer (colored red) and is the lowest at the far field (colored blue)

4.3 Stability of Marangoni Propulsion

Controlling the motion of Marangoni surfers requires a fundamental understanding of their stability, especially at high Reynolds numbers when the vortical structures in

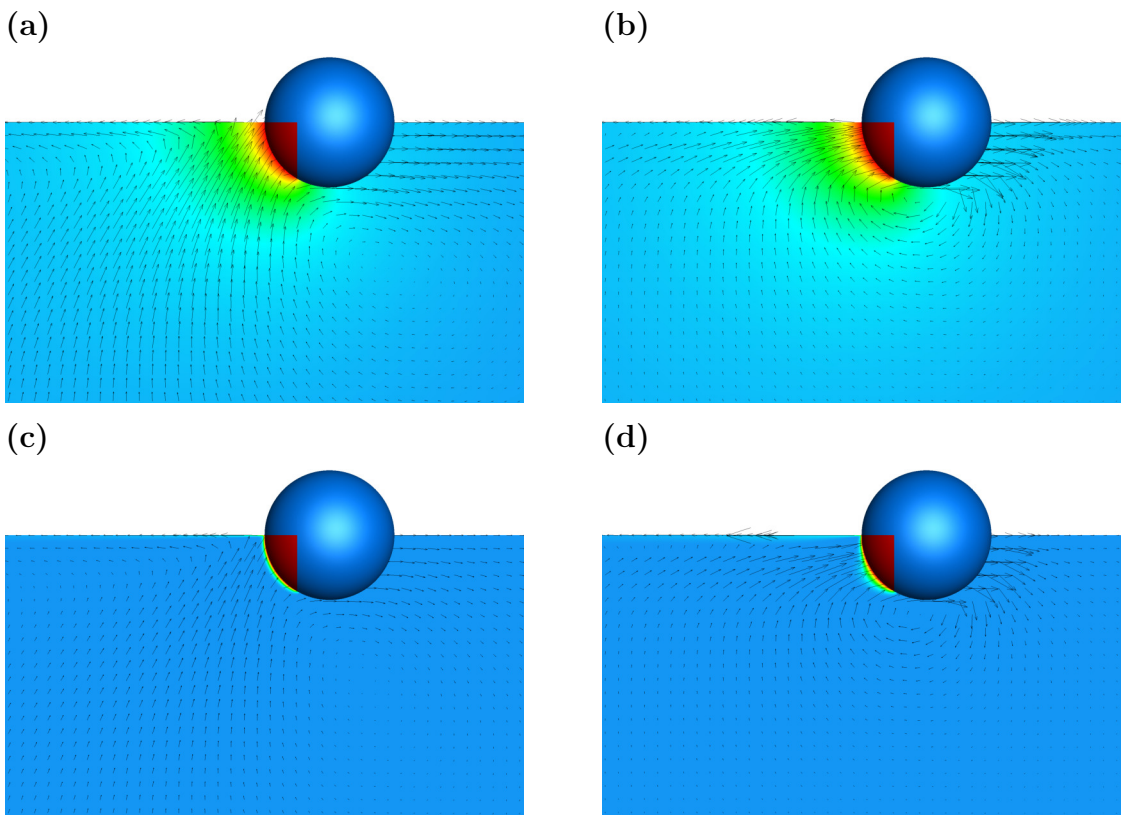

Figure 4.7: Velocity field and contour of active chemical concentration in the x-z plane bisecting the surfer corresponding to the Marangoni-driven motion of an active sphere at Re = 1 (left panel) and Re = 100 (right panel). The top and bottom rows show, respectively, the result at Pe = 0.1 and Pe = 1000. In the color maps the concentration is the highest at the active area of the surfer (colored red) and is the lowest at the far field (colored blue)

the vicinity of the surfers are noticeably strong. In these situations, disturbances that break the symmetry of the vortices might lead to the rotation and lateral movement of the particle and could cause it to drift from its intended path. In this section, we consider the translational stability of a spherical surfer in the absence of a confining wall.

To put the stability properties of the Marangoni surfer into context, we first

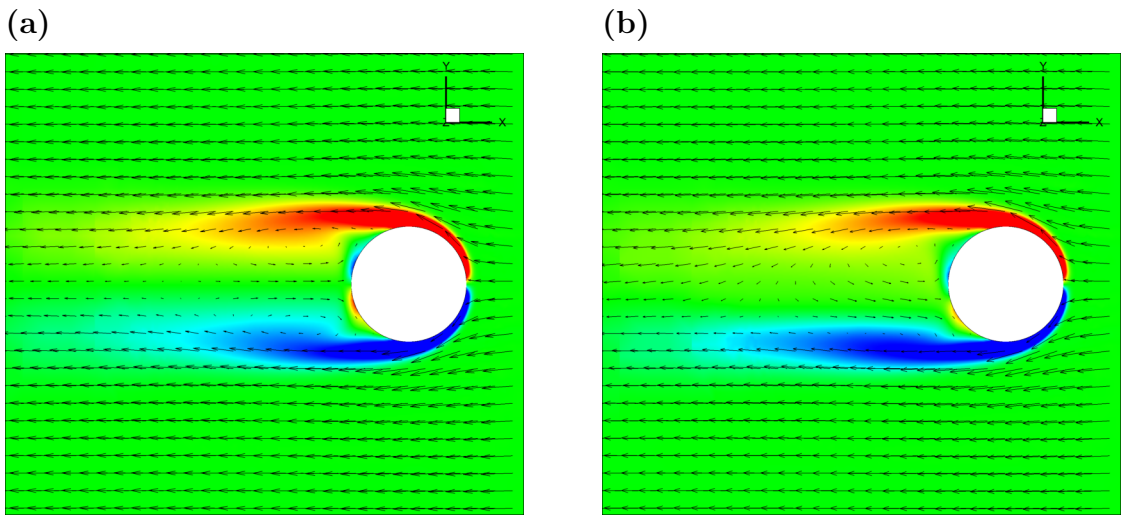

Figure 4.8: Interface vorticity and velocity vector field at (a) Re = 220 and (b) Re = 240, respectively, of a half-submerged inactive sphere at a water-air interface.

examine the stability of the same, but otherwise inactive, surfer. As we have mentioned before, the Marangoni propulsion of active surfers are due in part to a driving force which is the line integral of the surface tension over the three-phase contact line between the particle and the liquid-gas interface (see Eq. (3.5)). Hence, to mimic this motion for an inactive surfer sitting at an interface with no surface-tension variations (i.e., with zero shear-stress), we assume that the inert surfer is being pulled by a force that is always parallel to the interface and the force is attached to the surfer's local coordinate so it translates and rotates with it.

As the externally applied force increases, the steady-state speed (and, hence, the Reynolds number) becomes larger. At high enough Re, vortical structures emerge in the wake of the surfer (see Fig. 4.8). As Re further increases, the vortices become asymmetric and later begin shedding. In this scenario, if the surfer is not constrained

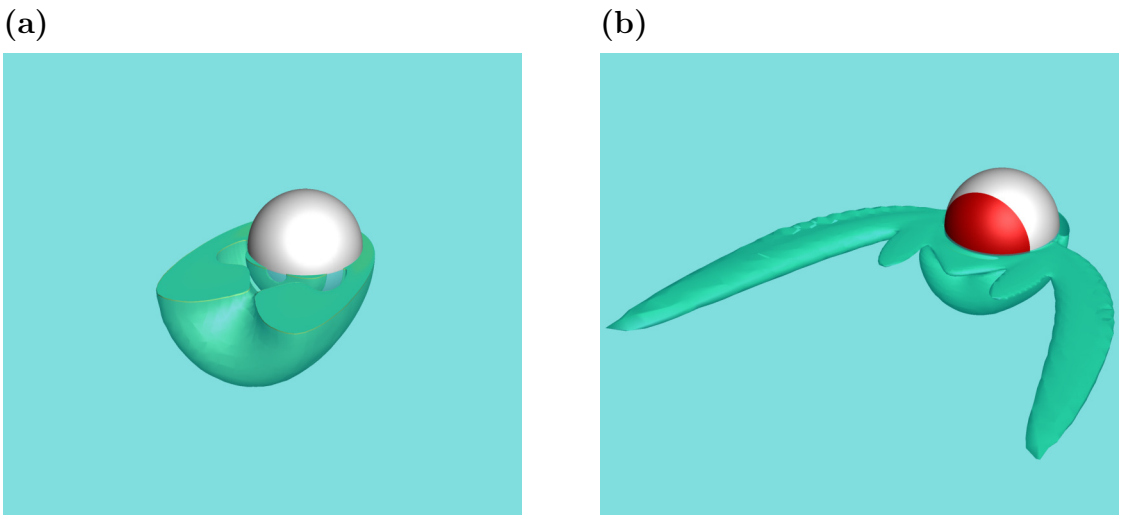

Figure 4.9: Q-criterion of (a) Translating inactive sphere located at zero-shear-stress interface at Re $\approx$ 220 and (b) Marangoni propulsion of active sphere at Re $\approx$ 240 and Pe = 1000, respectively.

to move along a straight line, it eventually starts to rotate and move along a curved path. Here, we seek to determine the minimum Re number at which the departure from the straight motion takes place. To this end, we let the sphere reach its steady-state speed (after applying the driving force) and then perturb its motion with a lateral velocity normal to the direction of the motion and parallel to the interface. The magnitude of the lateral velocity is set to approximately 5% of the steady-state speed. The perturbation is applied for a short period of time such that the maximum lateral displacement does not exceed 5% of the surfer's radius. We find that the surfer starts to wiggle around its line of motion at Re $\approx$ 125, and begins to rotate at Re $\approx$ 150.

Now that we have determined when the passive surfer becomes unstable, we consider the stability of the active one by repeating the same type of simulations for

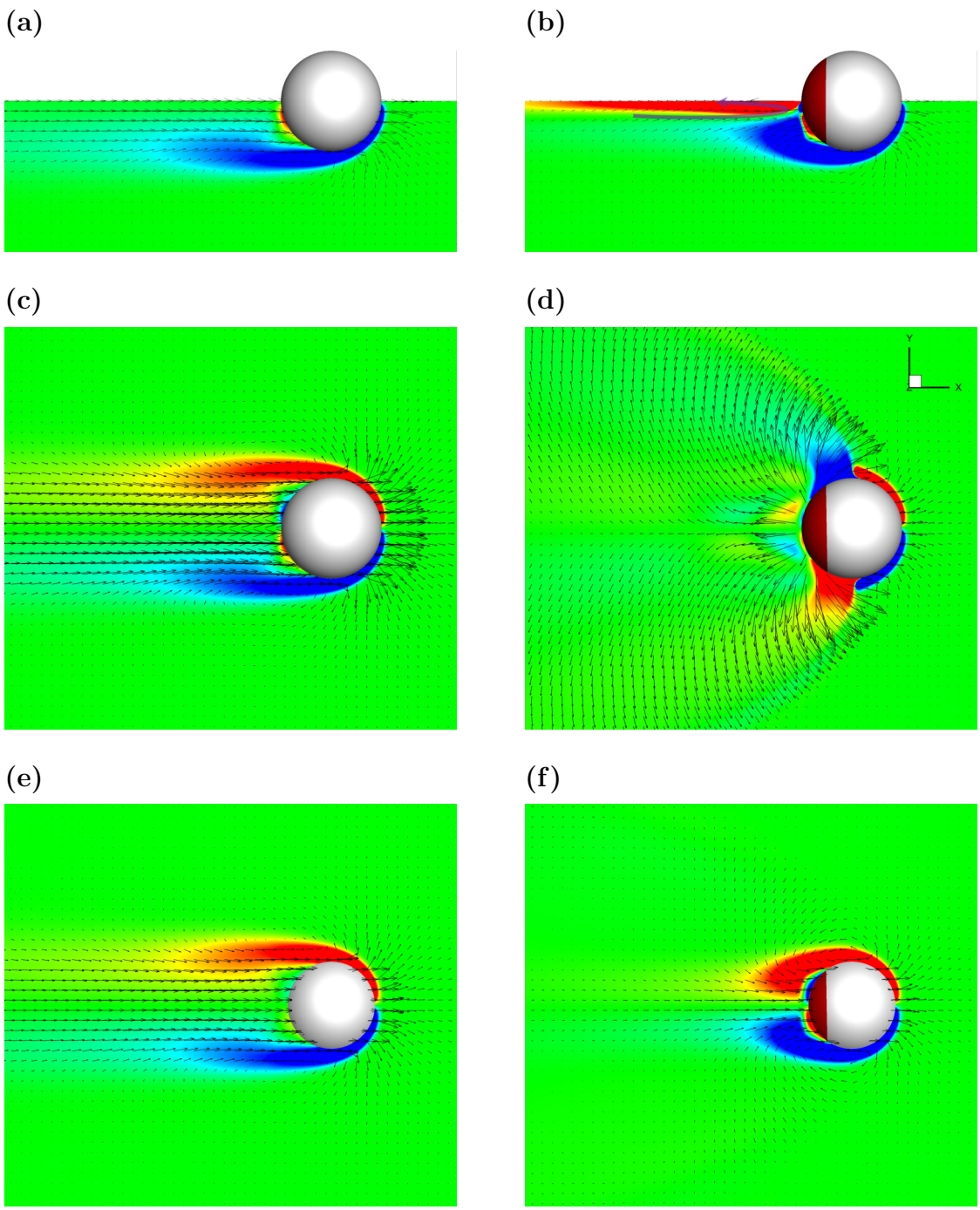

Figure 4.10: Vorticity field and velocity vector field (a,b) below the sphere (c,d) at interface (e,f) at $z = -R/2$ plane for Translating inactive sphere (left column Re ≈ 220) and Marangoni propulsion (right column Re ≈ 240 and Pe ≈ 1000). Vorticity fields are normalized by $2U/R$ and the range is from -1 to 1

$d = R/2$ and various Péclet numbers. Perhaps surprisingly, our simulations indicate that, irrespective of Pe, the active surfer tends to stay on course at Reynolds numbers up to Re ≈ 240. After that, when Re ≈ 300, the surfer starts rotating and becomes unstable. This suggests that the active surfer is more stable than an inactive one moving at the same speed. The difference in the critical Re can be attributed to the structure of the vorticity field in the wake of the active surfer, where the reverse flow behind the surfer helps keeping the vortices attached (see Figs. 4.10 and 4.9b).

4.4 Reverse Marangoni Propulsion

In chapter 2, we theoretically investigated the effect of wall confinement on the propulsion speed, and discovered that, depending on the shape of the surfer, when the liquid layer is shallow enough, the reverse propulsion occurs. However, the theory only covers the limit of negligible inertia and diffusion-dominated transport of the active agent. Here, we continue our investigation into the influence of the depth of the liquid layer on the propulsion speed when the Reynolds and Péclet numbers are no longer small.

4.4.1 Comparison Between Numerical and Experimental Results

We begin by comparing the results of our simulations with the experimental measurements reported in [81]. The experiments involve a cylindrical disk of radius $R = 2.25\,\text{mm}$ and thickness $\lambda = 1.5\,\text{mm}$, and a hemisphere of radius $R = 2.375\,\text{mm}$,

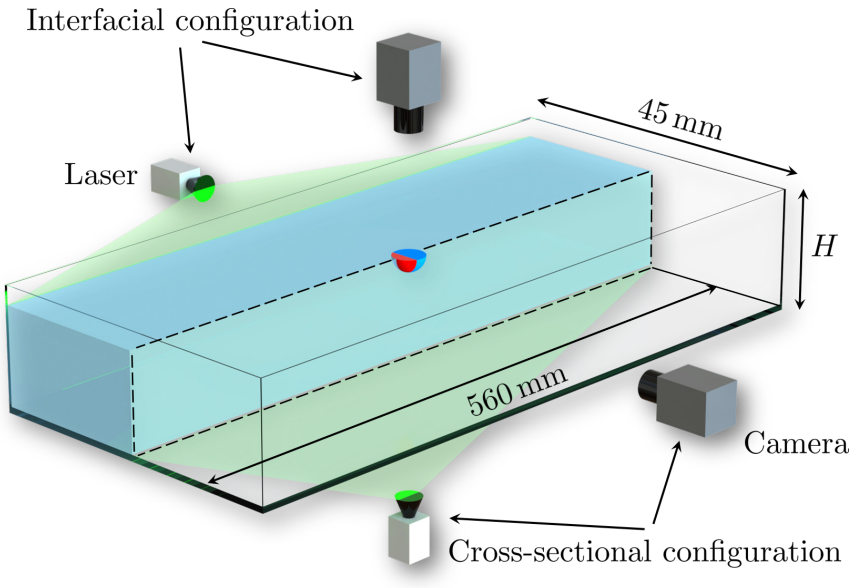

Figure 4.11: Schematics of the experimental setup depicting a fully submerged hemispherical surfer at a water-air interface. The area of the hemisphere dip-coated with a layer of Dawn soap that is colored red.

both from polydimethlysiloxane, which has a density of $\rho = 965\,\mathrm{Kg/m^3}$. The disk and hemisphere are dip-coated into a solution of water and 50% soap (Dawn) to a depth of $d = 1\,\mathrm{mm}$, as shown in Fig. 4.11. This process results in an asymmetric coating of the surfer with a layer of an active agent (i.e. Dawn soap), which is known to reduce the interfacial tension of water from $72\,\mathrm{mN/m}$ to about $30\,\mathrm{mN/m}$ [97]. The disk or hemisphere is gently placed on the water-air interface and released using tweezers. The dissolution of the coating layer creates a surface tension imbalance that, in turn, leads to the propulsion of the surfer. The experiments are conducted in a clear-walled rectangular container of length $L = 560\,\mathrm{mm}$ and width $W = 45\,\mathrm{mm}$, that is filled with water (see Fig. 4.11). The depth of water is varied from $H = 1.8\,\mathrm{mm}$ to $H = 10\,\mathrm{mm}$.

A particle image velocimetry is used to analyze the flow field at the water-air

interface and beneath the surfer. PIV measurements are performed using uniformly dispersed tracer particles of 40-μm diameter that are illuminated by a 300-mW argon-ion laser light sheet of thickness 1 mm. The laser is oriented either parallel to the interface just below the surface (in order to obtain the interfacial velocity profiles) or normal to the surface passing up through the fluid from the bottom of the container (see Fig. 4.11). Through this second configuration, the velocity field underneath the surfer is measured. A high speed camera at a maximum frame rate of 110 fps is utilized to capture the images, which are then processed via a commercial PIV software package developed by LaVision. Also, a digital camera is used to track the motion of the surfer. The videos are captured at 17 fps and fed into a particle tracking software (Tracker) to measure the speed and direction of the surfer's propulsion.

To analyze the propulsion behavior of a surfer, we measure its steady-state velocity U under various levels of confinement, characterized by the depth of the liquid layer H. Next, we normalize U by its corresponding value for deep layers (i.e. $H \to \infty$), denoted as U_∞, and plot the results versus $\delta/R = (H - \lambda)/R$. Here, δ and λ are the minimum gap between the surfer and the confining wall, and the thickness of the submerged volume of the surfer, respectively. In view of the simplifying assumptions enumerated in the earlier chapters, the quantity U/U_∞ is a function of the shape of the surfer and δ/R, as well as the Reynolds and Péclet numbers. These two parameters are defined, respectively, as

$$\mathrm{Re} = 2\rho U_\infty R/\mu \quad \text{and} \quad \mathrm{Pe} = 2 U_\infty R/\mathcal{D},$$

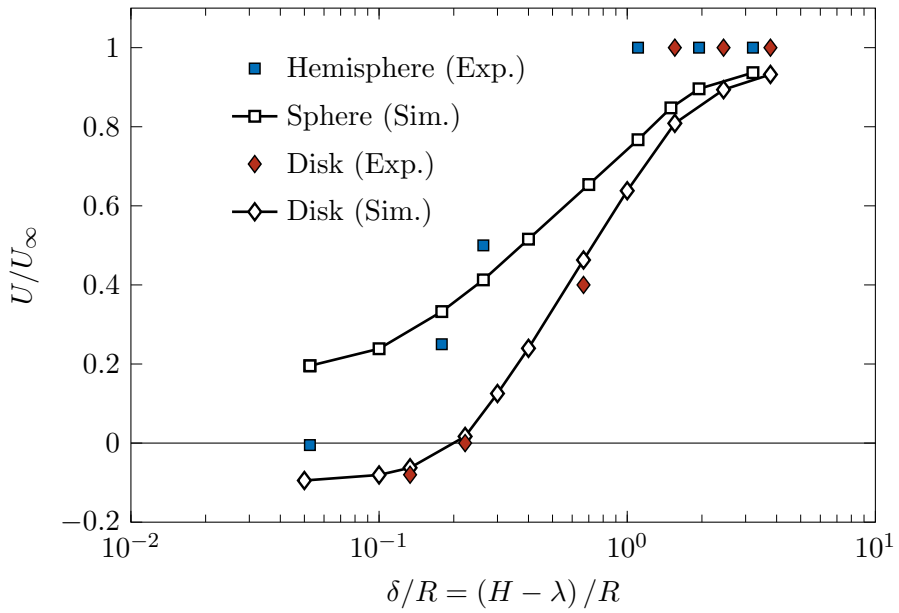

Figure 4.12: Comparison between the results of experimental measurements (filled symbols) and numerical calculations (empty symbols) for the normalized propulsion velocity U/U_∞ versus the dimensionless minimum gap between the surfer and the confining wall δ/R. The Reynolds numbers corresponding to the motion of the sphere/hemishpere (square symbols) and disk (diamond symbols) are $\mathrm{Re} \approx 23$ and $\mathrm{Re} \approx 25$, respectively. The Péclet number is of the order of $\mathrm{Pe} \sim \mathcal{O}(10^5)$ in the experiments and is set to $\mathrm{Pe} \approx 1000$ in the simulations, which is sufficiently high to justify the comparison.

in this section, where U_∞ is used as the characteristic velocity instead of $U^\star$.

Figure 4.12 shows the variation of the normalized propulsion velocity U/U_∞ as a function of the dimensionless minimum gap between the surfer and the confining wall δ/R, where the experimental and numerical data points are distinguished by the filled and empty symbols, respectively. The Reynolds numbers corresponding to the motion of the sphere/hemisphere (square symbols) and disk (diamond symbols) are $\mathrm{Re} \approx 23$ and $\mathrm{Re} \approx 25$, respectively. The Péclet numbers, on the other hand, are of the order of $\mathrm{Pe} \sim \mathcal{O}(10^5)$ in the experiments and are set to $\mathrm{Pe} \approx 1000$ in the simulations, which is believed to be high enough to justify the comparison.

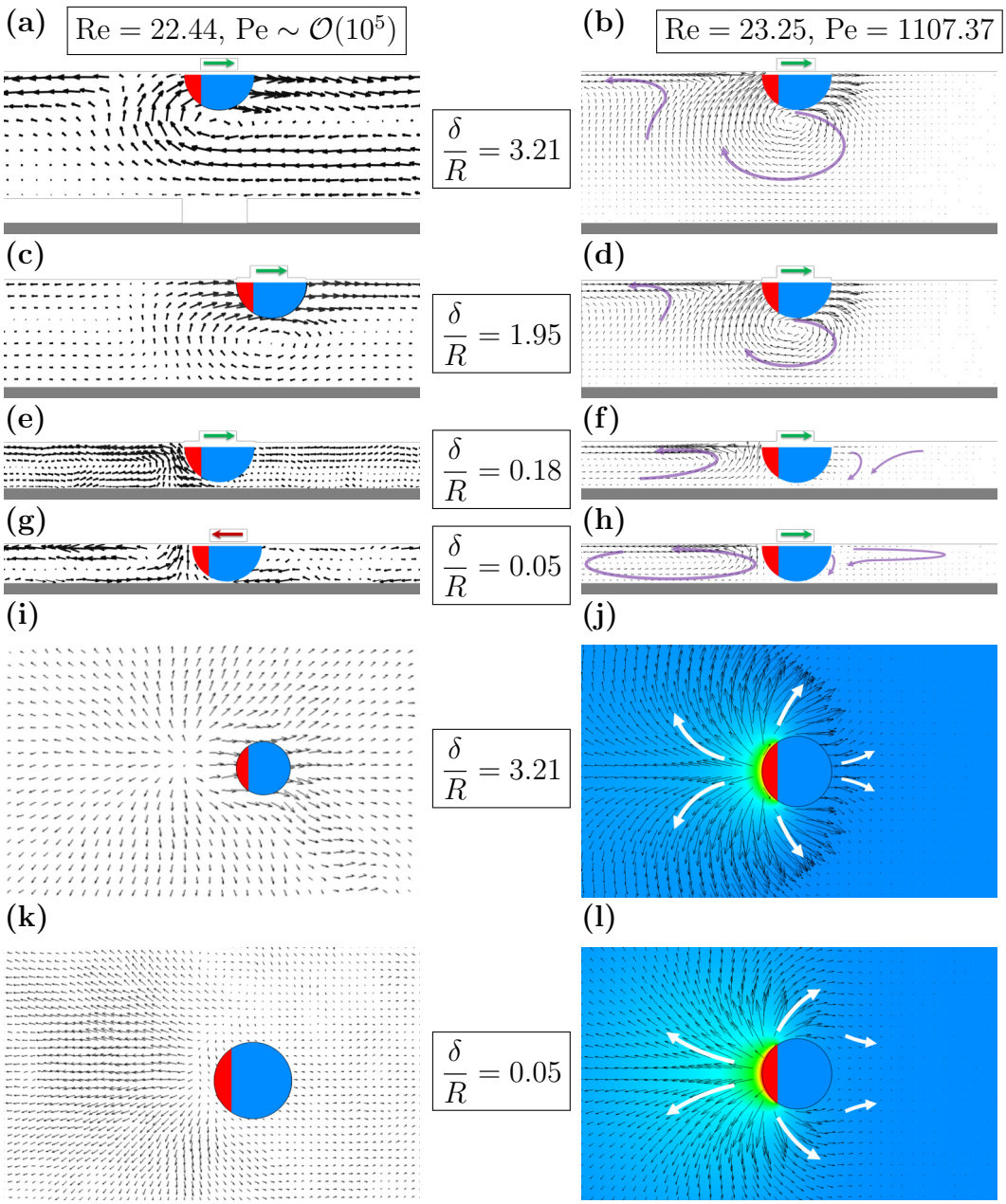

Figure 4.13: Flow field plots corresponding to the Marangoni propulsion of a hemisphere/-sphere under various degrees of confinement for PIV measurements (left panels) and numerical simulations (right panels). The top four rows show the fluid flow in the x-z plane bisecting the surfer, and the fifth and sixth rows illustrate the velocity field at the water-air interface for, respectively, the least and most confined cases (i.e. the first and fourth rows). In the right panels, the thick arrows highlight the direction of the flow and the color maps display the concentration distribution of the active agent, where the concentration is the highest at the active area of the surfer (colored red) and is the lowest at the far-field (colored blue). The black arrows are scaled independently in each panel to facilitate flow visualization. The red and green arrows atop each panel show the direction of propulsion.

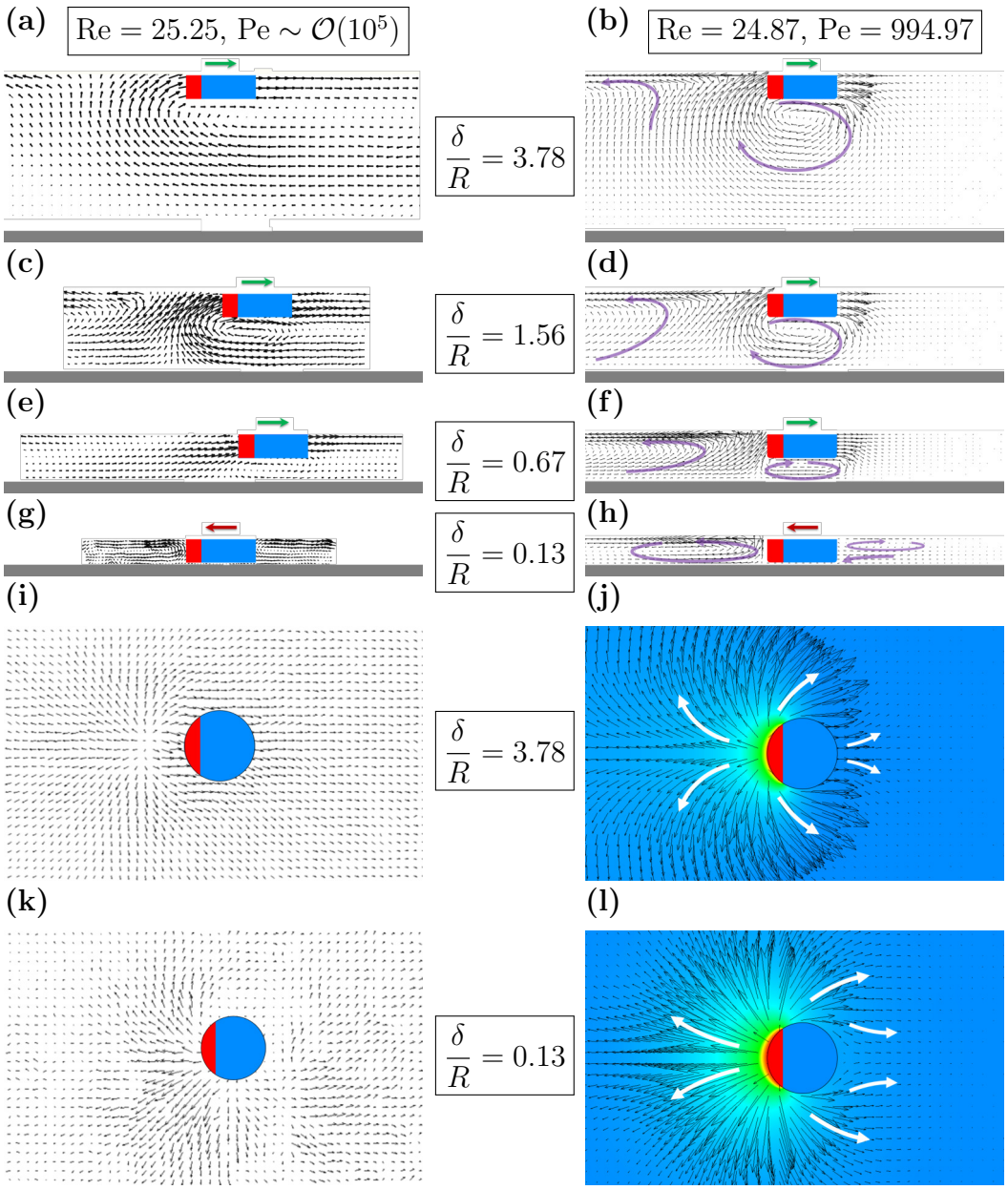

Figure 4.14: Flow field plots corresponding to the Marangoni propulsion of a disk under various degrees of confinement for PIV measurements (left panels) and numerical simulations (right panels). The top four rows show the fluid flow in the x-z plane bisecting the surfer, and the fifth and sixth rows illustrate the velocity field at the water-air interface for, respectively, the least and most confined cases (i.e. the first and fourth rows). In the right panels, the thick arrows highlight the direction of the flow and the color maps display the concentration distribution of the active agent, where the concentration is the highest at the active area of the surfer (colored red) and is the lowest at the far-field (colored blue). The black arrows are scaled independently in each panel to facilitate flow visualization. The red and green arrows atop each panel show the direction of propulsion.

We see that, in all cases, once the gap is greater than several particle radii, the propulsion velocity asymptotes to U_∞ and is no longer affected by the bounding wall underneath the water-air interface. As the gap decreases and begins to approach the radius of the surfer (i.e. $\delta/R \approx 1$), the confinement effect kicks in, which notably slows down the speed of the surfer. On further narrowing the gap, for experimentally tested surfers (see filled symbols), this trend continues until the surfer comes to rest – even though the fluid around it continues to flow. Beyond this critical point, the surfer reverses its course. The magnitude of the reverse velocity and the crossover depth are functions of, among other factors, the geometry of the surfer and, therefore, differ for the hemisphere and disk. Specifically, a comparison between the plots for the sphere and disk (filled squares and diamonds in Fig. 4.12) reveals that the gap corresponding to the onset of backward propulsion is several times thinner for the sphere. Furthermore, the maximum rearward speed of the sphere is about an order of magnitude slower than that of the disk, which is about 10% of its U_∞.

The above experimental observations are largely corroborated by the numerical calculations (see empty symbols), with the exception that, in the simulations, the velocity of the spherical surfer approaches a finite positive value at very small gaps (i.e. $\delta/R \ll 1$). This discrepancy can be attributed to the decay in the release rate of the soap coating with time (which can lead to uncertainty in determining the precise experimental Reynolds number), the local increase in the water viscosity due to the release of the soap from the surface of the sphere, and also the pitching motion of the

hemisphere (due to the net torque exerted on its wetted surface) in the experiments. In the next subsection, we will show that the reverse motion for spherical surfers occurs at Reynolds numbers Re $\lessapprox$ 10 in our idealized model.

Figures 4.13 and 4.14 illustrate the flow structure near the Marangoni surfer for representative data points in Fig. 4.12. We see that the results of PIV experiments (left columns) agree favorably with those of numerical simulations (right columns), and they both depict the following physical picture. In section §4.2, we discussed the flow patterns below the interface and near the surfer. Here, when the wall is far enough from the surfer, the flow structure is the same (see Figs. 4.13b, 4.13j, 4.14b, 4.14j,). As the thickness of the liquid layer decreases, however, the counterclockwise rotating vortex in the wake of the surfer becomes more shallow, with its center moving towards the interface and closer to the stagnation point. And, the clockwise rotating vortex gets compressed and weakened until it disappears upon further reducing the depth of water (see the fourth rows of Figs. 4.13 and 4.14). In this situation, a narrow clockwise rotating vortex emerges next to the surfer, opposite to its active side (see the third and fourth rows of Fig. 4.13 and the fourth row of Fig. 4.14). This flow feature is more distinct for the case of the disk.

4.4.2 Additional Numerical Calculations

Having further demonstrated the credibility of our computational approach, we now use numerical modeling to examine the effects of the Reynolds and Péclet numbers as

well as the surfer's geometry on Marangoni propulsion under confinement. To this end, we simulate the surfing motion of oblate spheroids with aspect ratios $\varepsilon = 1,\ 0.5,\ 0.2$ at $\mathrm{Re} \approx 0.1,\ 1,\ 10,\ 100$ and $\mathrm{Pe} \approx 0.1,\ 10,\ 1000$. In these simulations, we set $d = R/2$, and increase the length and width of the domain to $L = 100R$ and $W = 50R$ to lessen the influence of the side boundaries. The plots of U/U_∞ versus δ/R for each Reynolds number at $\mathrm{Pe} \approx 1000$ are displayed in Fig. 4.15. The results for $\mathrm{Re} \approx 0.1$ and $\mathrm{Re} \approx 1$

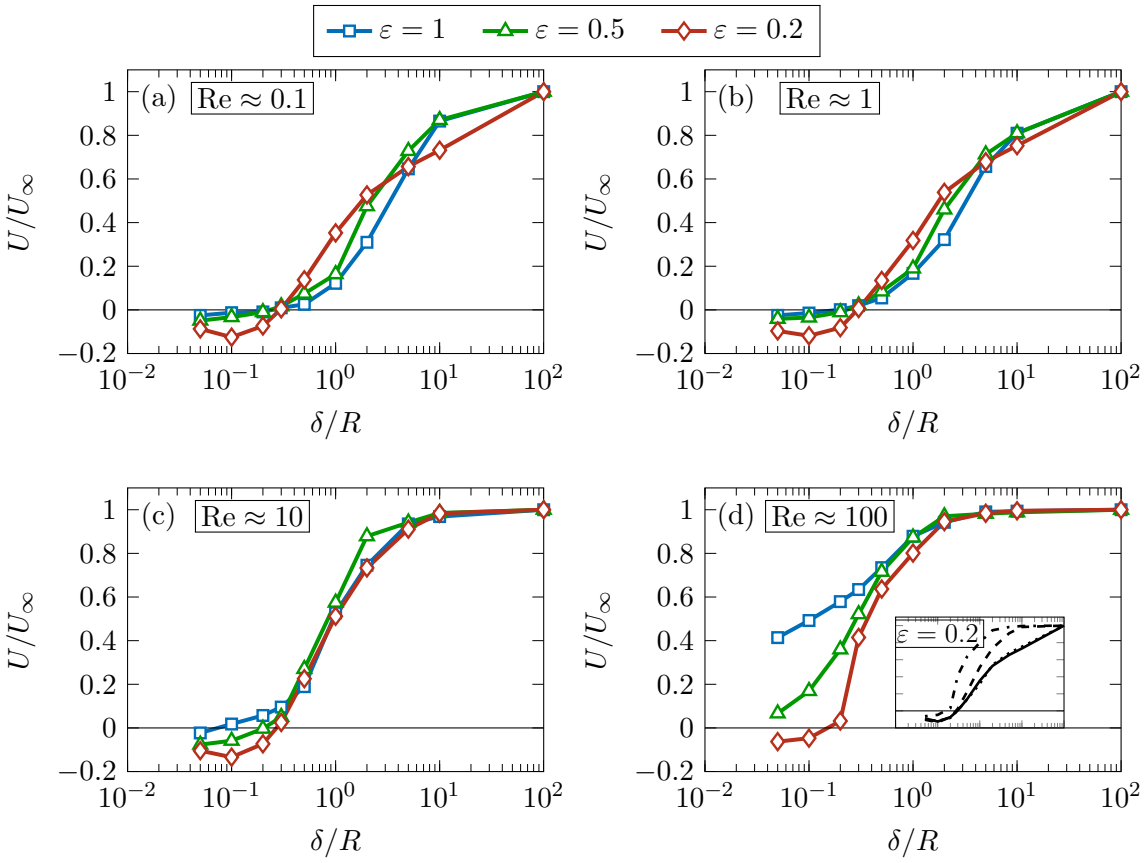

Figure 4.15: Normalized propulsion velocity U/U_∞ versus the dimensionless minimum gap between the surfer and the confining wall δ/R. The results are shown for $\mathrm{Pe} \approx 1000$ and half-submerged oblate spheroidal surfers of aspect ratio $\varepsilon = 1, 0.5,$ and 0.2. Panels (a)–(d) correspond to $\mathrm{Re} \approx 0.1, 1, 10,$ and 100, respectively. The inset in panel (d) shows the replots of U/U_∞ vs. δ/R curves for $\varepsilon = 0.2$ from panels (a)–(d).

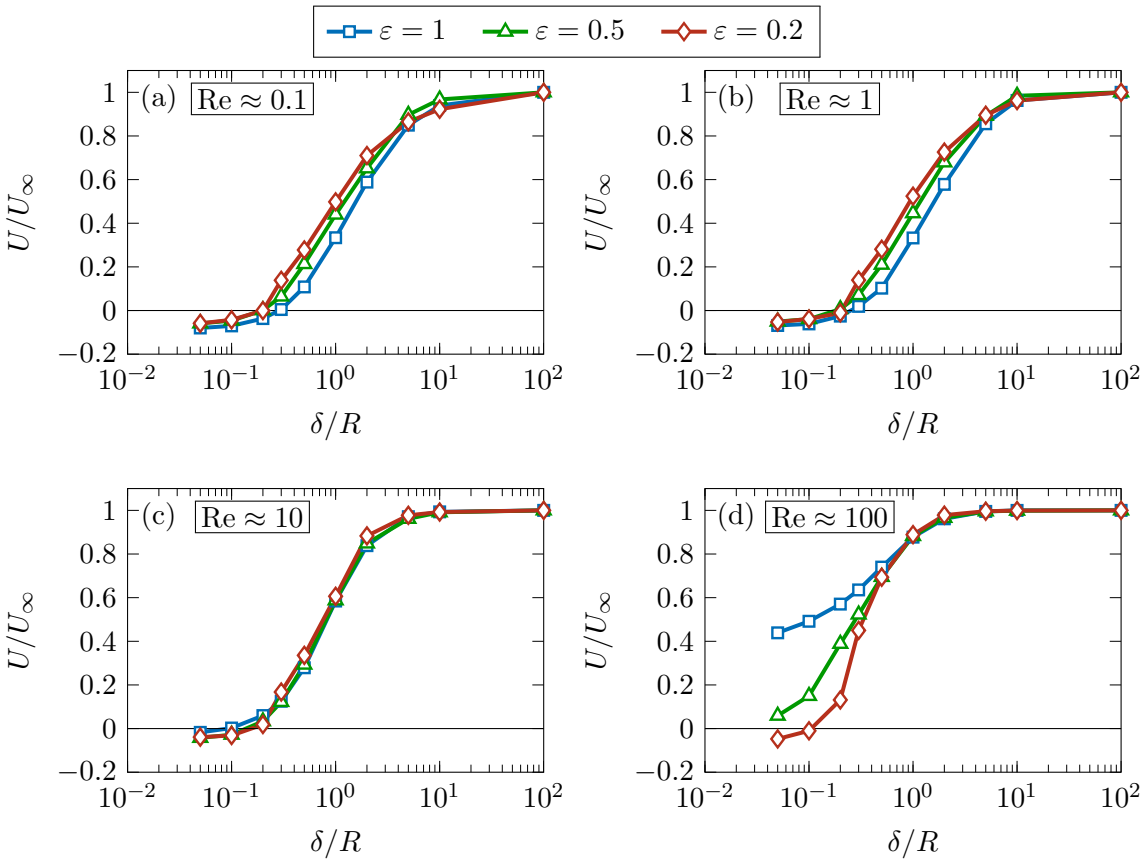

Figure 4.16: Normalized propulsion velocity U/U_∞ versus the dimensionless minimum gap between the surfer and the confining wall δ/R. The results are shown for Pe $\approx$ 10 and half-submerged oblate spheroidal surfers of aspect ratio $\varepsilon = 1, 0.5,$ and 0.2. Panels (a)–(d) correspond to Re $\approx 0.1, 1, 10,$ and 100, respectively.

are quite alike and they both indicate that all surfers experience the reverse Marangoni propulsion when the liquid layer is sufficiently confined. Specifically, the crossover gap is $\delta/R \approx 0.25$ for $\varepsilon = 1$ (spherical surfer) and $\varepsilon = 0.5$ whereas it is closer to $\delta/R \approx 0.3$ for $\varepsilon = 0.2$ (see Figs. 4.15a and 4.15b). Also, in all cases, the reverse speed is about or less than 15% of its respective U_∞. At the moderate Reynolds number of Re $\approx$ 10, we still observe analogous trends, with thicker surfers transitioning from forward to backward motion at narrower gaps (see Fig. 4.15c). This observation corroborates

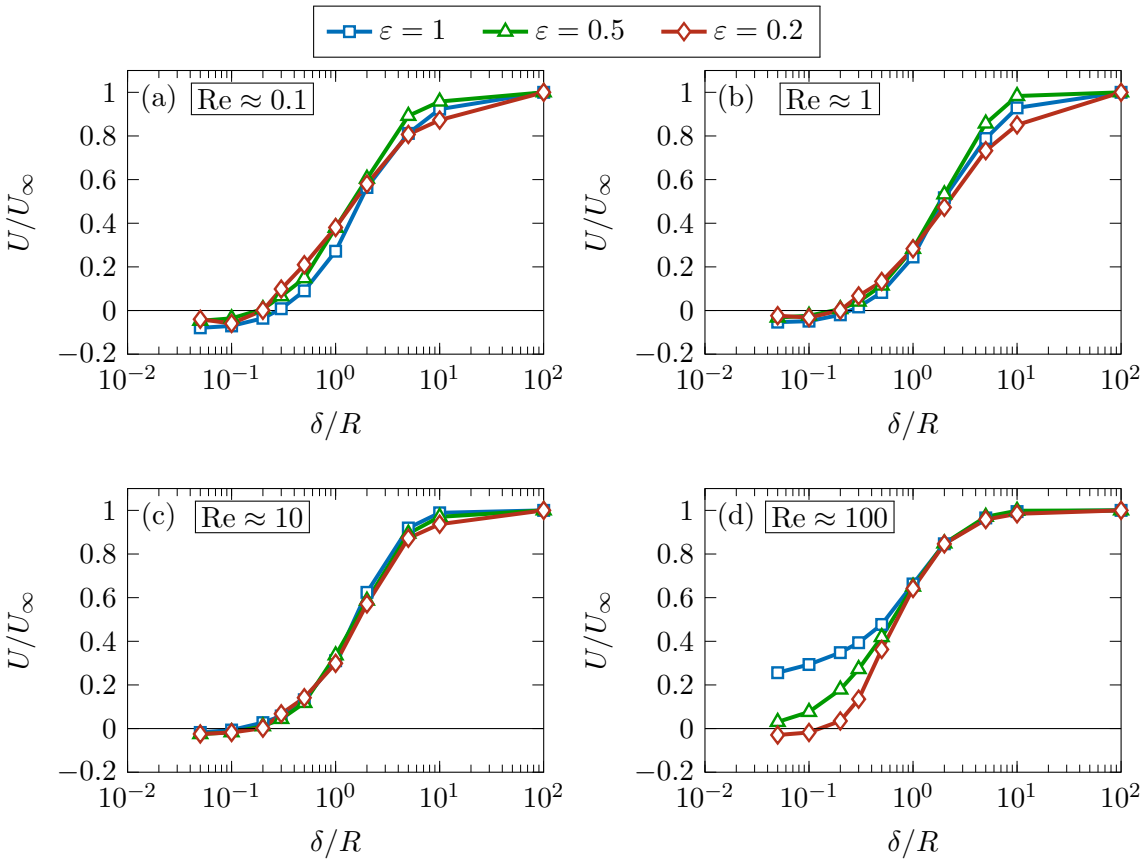

Figure 4.17: Normalized propulsion velocity U/U_∞ versus the dimensionless minimum gap between the surfer and the confining wall δ/R. The results are shown for Pe ≈ 0.1 and half-submerged oblate spheroidal surfers of aspect ratio $\varepsilon = 1, 0.5,$ and 0.2. Panels (a)–(d) correspond to Re $\approx 0.1, 1, 10,$ and 100, respectively.

well with the experimental measurements presented in Fig. 4.12.

When Re is raised by another order of magnitude, however, major changes occur in the propulsion behavior of surfers with moderate to high aspect ratios (see Fig. 4.15d). In particular, for the cases with $\varepsilon = 1$ and $\varepsilon = 0.5$, lowering of the gap no longer alters the propulsion direction. Remarkably, for the spherical surfer, U/U_∞ drops to only about 0.4 at the very small gap size of $\delta/R = 0.05$. Overall, we find that, for the range of Re considered, the general behavior of U/U_∞ vs δ/R curves is

less sensitive to the Reynolds number for low aspect ratio surfers (see the inset in Fig. 4.15d for $\varepsilon = 0.2$). This could explain why numerical and experimental results matched more closely for the disk in Fig. 4.12, despite the uncertainty in the actual value of Re in the experiments.

Figures 4.17 and 4.16 present the plots of U/U_∞ versus δ/R for, respectively, Pe = 10 and Pe = 0.1. Comparing these figures against Fig. 4.15 shows that while *pe* is varied over four orders of magnitude, the results for the normalized speed for different δ/R and Re remain fairly similar. This suggests that the effect of the Péclet number on the surfing speed on top of a finite-depth liquid layer is less significant that the influences of the surfer's geometry and the Reynolds number.

The data in Figs. 4.15, 4.16, and 4.17 correspond to the steady-state motion of the surfers. In this condition, the net force acting on the particle in the direction of propulsion is zero, which means that the surface tension force $F_{st} = \boldsymbol{e}_x \cdot \int_{\ell_p} \gamma \boldsymbol{t} \, \mathrm{d}\ell$ is balanced by the sum of pressure and viscous forces $F_p + F_v = F = \boldsymbol{e}_x \cdot \int_{S_p} \boldsymbol{n} \cdot \boldsymbol{\sigma} \, \mathrm{d}S$ (see Eq. (3.5)). Given the orientation of the (x, y, z) coordinate system with respect to the location of S_p^a, F_{st} is always a positive quantity (see Fig. 3.1b). Of fundamental interest here are the relative contributions of pressure and viscous forces. It is also of value to have an understanding about the distribution of the forces over S_p. For instance, it is informative to know, if the surfer is divided into two equal halves, say active (which encompasses the release site) and inactive, how F_p, F_v, and their sum F would split between these two regions. Table 4.1 provides this information for

illustrative points in Fig. 4.15, where the forces and their subdivisions (denoted by the superscripts a and ia) are normalized by F_{st}.

First, we discover that, in the vast majority of cases considered, much of the resistance to the surface tension force is due to the negative pressure (suction) exerted on the active half of the surfer F_p^a; the far-field pressure is set to zero in the simulations. The rest of the resistance comes from the viscous force F_v (which is more evenly split over S_p than F_p) and the pressure force acting on the inactive side of the surfer F_p^{ia}. The share of the latter is often very small. Consider, for example, the case of $\varepsilon = 0.5$, $\delta/R = 0.5$, and $\mathrm{Re} \approx 10$, for which $F_p/F_{st} = -0.69$ and $F_v/F_{st} = -0.31$, or a more extreme case of $\varepsilon = 1$, $\delta/R = 0.05$, and $\mathrm{Re} \approx 100$, with $F_p/F_{st} = -0.89$ and $F_v/F_{st} = -0.11$. To put these force decompositions into perspective, 2/3 of the Stokes drag on a moving sphere comes from the viscous stresses and the remainder is the contribution of the pressure. And, the pressure drags felt on the front and back sides of the sphere are identical. Our calculations indicate that the relative contribution of F_p^a (and consequently that of F_p) increases with reducing the gap size and decreases mildly with the rise of inertial effects. They also show that F_p/F_{st} is greater for more rounded surfers.

Second, we learn that there exists a link between the direction of surfers' motion and the distribution of the total fluid force on their active and inactive halves. Specifically, we find that the reverse Marangoni propulsion is associated with the fluid force

Re ≈ 10										
ε	$\frac{\delta}{R}$	$\frac{U}{U_\infty}$	$\frac{F^a}{F_{st}}$	$\frac{F^{ia}}{F_{st}}$	$\frac{F_p}{F_{st}}$	$\frac{F_v}{F_{st}}$	$\frac{F_p^a}{F_{st}}$	$\frac{F_p^{ia}}{F_{st}}$	$\frac{F_v^a}{F_{st}}$	$\frac{F_v^{ia}}{F_{st}}$
1	5	0.93	−0.85	−0.15	−0.74	−0.26	−0.70	−0.04	−0.15	−0.11
	0.5	0.19	−0.95	−0.05	−0.79	−0.21	−0.80	0.01	−0.15	−0.06
	0.05	−0.02	−1.12	0.12	−0.89	−0.11	−1.03	0.14	−0.09	−0.02
0.5	5	0.94	−0.81	−0.19	−0.61	−0.39	−0.57	−0.04	−0.24	−0.15
	0.5	0.27	−0.90	−0.10	−0.69	−0.31	−0.68	−0.01	−0.22	−0.09
	0.05	−0.08	−1.21	0.21	−0.86	−0.14	−1.10	0.24	−0.11	−0.03
0.2	5	0.91	−0.77	−0.23	−0.40	−0.60	−0.38	−0.02	−0.39	−0.21
	0.5	0.23	−0.86	−0.14	−0.48	−0.52	−0.48	0.00	−0.38	−0.14
	0.05	−0.10	−1.16	0.16	−0.84	−0.16	−0.94	0.10	−0.22	0.06
Re ≈ 100										
ε	$\frac{\delta}{R}$	$\frac{U}{U_\infty}$	$\frac{F^a}{F_{st}}$	$\frac{F^{ia}}{F_{st}}$	$\frac{F_p}{F_{st}}$	$\frac{F_v}{F_{st}}$	$\frac{F_p^a}{F_{st}}$	$\frac{F_p^{ia}}{F_{st}}$	$\frac{F_v^a}{F_{st}}$	$\frac{F_v^{ia}}{F_{st}}$
1	5	0.99	−0.76	−0.24	−0.70	−0.30	−0.66	−0.04	−0.10	−0.20
	0.5	0.73	−0.83	−0.17	−0.73	−0.27	−0.73	0.00	−0.10	−0.17
	0.05	0.41	−0.89	−0.11	−0.80	−0.20	−0.81	0.01	−0.08	−0.12
0.5	5	0.98	−0.79	−0.21	−0.59	−0.41	−0.55	−0.04	−0.24	−0.17
	0.5	0.72	−0.83	−0.17	−0.66	−0.34	−0.64	−0.02	−0.19	−0.15
	0.05	0.07	−0.93	−0.07	−0.77	−0.23	−0.78	0.01	−0.15	−0.08
0.2	5	0.98	−0.65	−0.35	−0.39	−0.61	−0.36	−0.03	−0.29	−0.32
	0.5	0.64	−0.74	−0.26	−0.44	−0.56	−0.44	0.00	−0.30	−0.26
	0.05	−0.06	−1.07	0.07	−0.77	−0.23	−0.84	0.07	−0.23	0.00

Table 4.1: Decomposition of the fluid force acting on the surfer for illustrative data points in Figs. 4.15c and 4.15d. The subscripts p and v denote the contributions of pressure and viscous forces, respectively. The surfer is assumed to consist of two equal halves, active (which encompasses the release site) and inactive. And, the forces exerted on these regions are distinguished by the superscripts a and ia, respectively. All forces are normalized by the surface tension force $F_{st} = \boldsymbol{e}_x \cdot \int_{\ell_p} \gamma \boldsymbol{t}\, \mathrm{d}\ell$, which is equal to the negative of $F = \boldsymbol{e}_x \cdot \int_{S_p} \boldsymbol{n} \cdot \boldsymbol{\sigma}\, \mathrm{d}S = F_p + F_v = F^a + F^{ia}$ with $F_p = F_p^a + F_p^{ia}$, $F_v = F_v^a + F_v^{ia}$, $F^a = F_p^a + F_v^a$, and $F^{ia} = F_p^{ia} + F_v^{ia}$.

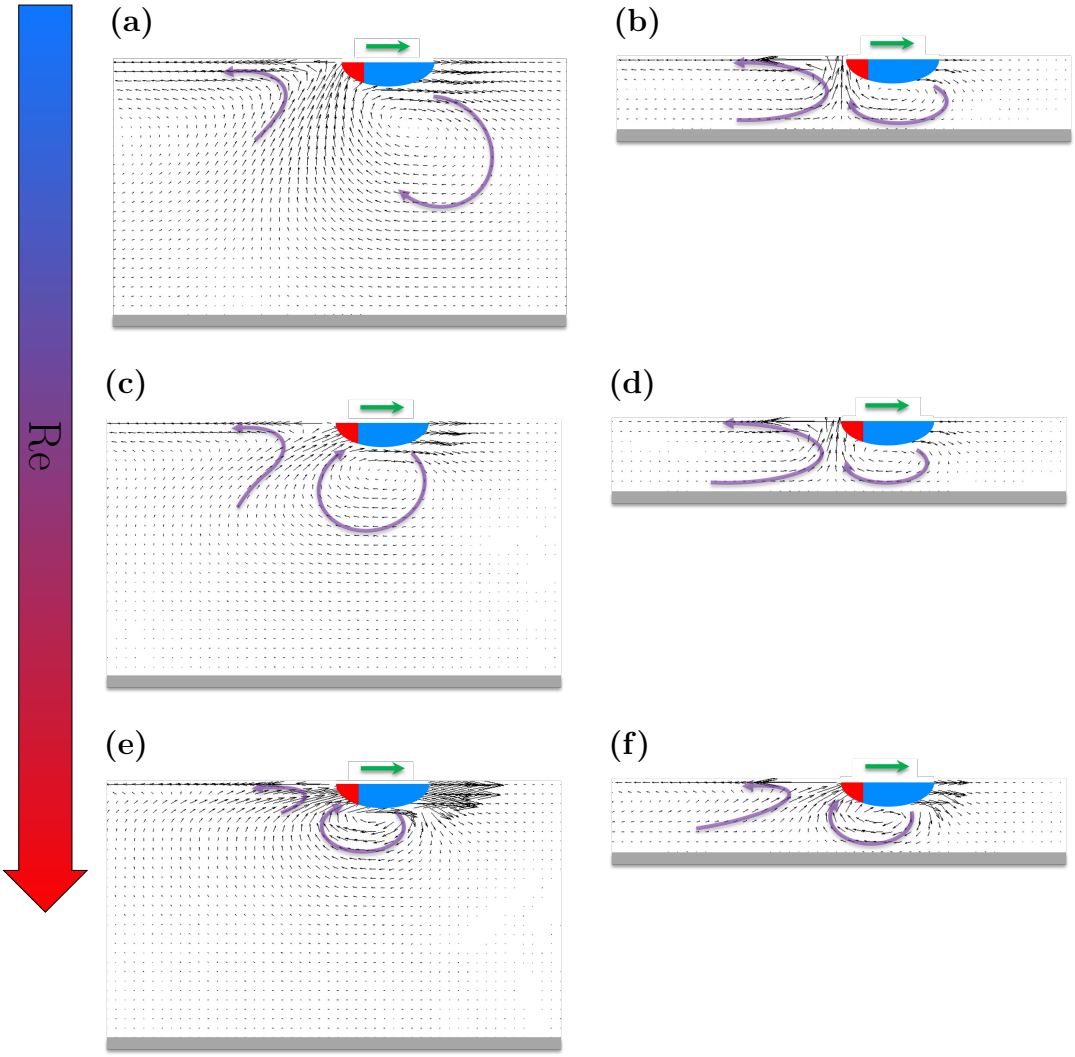

Figure 4.18: Flow field plots corresponding to the Marangoni propulsion of a half-submerged oblate spheroid of aspect ratio $\varepsilon = 0.5$. The results are produced from numerical simulations for Pe ≈ 1000 (see Fig. 4.15). The gap size is $\delta/R = 5$ and $\delta/R = 1$ in the left and right columns, respectively. The Reynolds number increases in each successive row from Re ≈ 1 to Re ≈ 10 and then to Re ≈ 100. The black arrows are scaled independently in each panel to facilitate flow visualization. The green arrows atop each panel show the direction of propulsion and the purple ones highlight the flow pattern.

on the active sides of a surfer exceeding that of the surface tension force in the negative direction ($F^a/F^{st} < -1$), which also corresponds to a positive value for the force

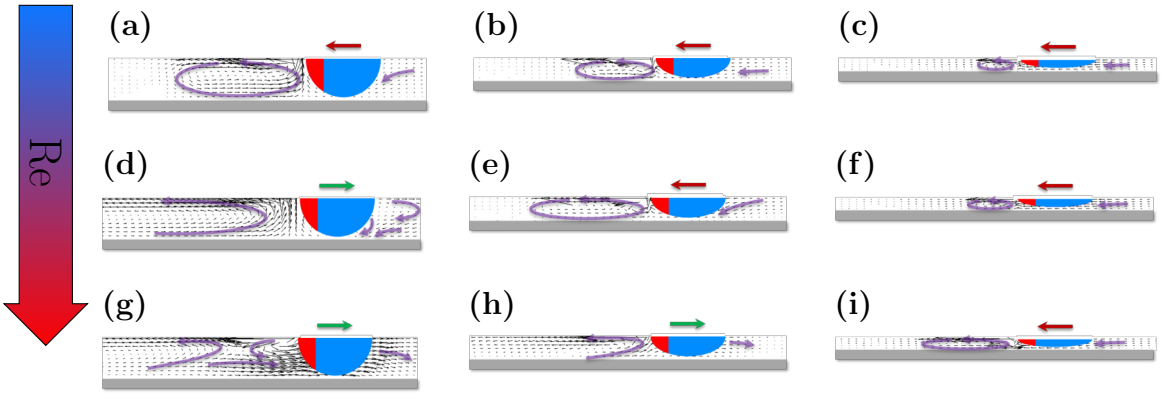

Figure 4.19: Flow field plots corresponding to the Marangoni propulsion of half-submerged oblate spheroids of various aspect ratios under extreme confinements ($\delta/R = 0.1$). The results are produced from numerical simulations for Pe ≈ 1000 (see Fig. 4.15). The left, middle, and right columns illustrate the flow for $\varepsilon = 1$, $\varepsilon = 0.5$, and $\varepsilon = 0.2$, respectively. The Reynolds number increases in each successive row from Re ≈ 1 to Re ≈ 10 and then to Re ≈ 100. The black arrows are scaled independently in each panel to facilitate flow visualization. The red and green arrows atop each panel show the direction of propulsion and the purple ones highlight the flow pattern.

on the inactive side of the surfer ($0 < F^{ia}/F^{st}$), see the boxes in Table 4.1. In other words, our force decomposition analysis suggests that once the sum of the suction and viscous forces on the active side of a surfer (which monotonically increases in magnitude with reducing the gap) outweighs the surface tension force then the surfer begins to move in the reverse direction. The change in the direction of motion results in the generation of a positive total force on the other (inactive) side of the surfer to compensate for the excess negative force on its active side, thereby maintaining a steady force balance. As a separate but related matter, we note that, for a given ε and Re, F_{st} is almost invariant to changes in δ/R. The two exceptions are when $\varepsilon = 1$ and $\varepsilon = 0.5$ for Re ≈ 10 and $\delta/R = 0.05$. In these cases a decrease of two orders of magnitude in the gap size results in 9% and 13% changes in F_{st}, respectively. By

contrast, in other cases the changes are 2% or less.

The results of Fig. 4.15 and Table 4.1 are supplemented by the flow field plots of Figs. 4.18 and 4.19, that show the variations of the flow pattern around the surfer with increasing Re at, respectively, low to moderate and extreme confinements. From Fig. 4.18, we learn that higher Re corresponds to more compact vortices, which is in line with intuition. Consistent with Figs. 4.13 and 4.14, we also see that the vortices are compressed as the liquid layer gets shallower. The choice of aspect ratio $\varepsilon = 0.5$ in this figure is immaterial, since the qualitative structure of the flow is insensitive to the thickness of the surfer. To the contrary, as shown in Fig. 4.19, when the gap is very thin, the surfer's aspect ratio plays a fundamental role in shaping the flow structure in its vicinity. It also affects how dependent the flow pattern is on Re. For instance, varying Re results in completely distinct flows for $\varepsilon = 1$ and nearly identical ones for $\varepsilon = 0.2$ (see the first and last columns of Fig. 4.19).

Before bringing this section to a close, we would like to briefly comment on how we have modeled the release of the chemical species. In its simplest form, the release process can be simulated by applying either a constant concentration or a constant flux boundary condition on S_p^a. Both of these conditions are capable of faithfully representing the emission of the chemical species, and they produce very similar results provided that their respective release rates match. Here, we have chosen to impose a *depth-invariant* constant concentration at S_p^a because it better mimics the way the

soap coating spreads in the experiments and also does not require *a priori* knowledge of the release rate. In chapter §2, where the reverse Marangoni propulsion was predicted theoretically in the limits of vanishing Re and Pe), on the other hand, a constant flux boundary condition was applied. There, it was assumed that the release rate of the active agent is fixed and does not change with the gap size. This subtle difference in modeling ought to be taken into account when comparing the results of Figs. 4.12, 4.15, 4.16, and 4.17 with those of Fig. 2.3.

Finally, it is worth noting that the reverse Marangoni surfing is not necessarily limited to self-propelling surfers. For example, Kavokine et al. [98] considered the transport of a liquid marble floating on a water-air interface embedding photosensitive surfactants. They observed that, when the liquid layer beneath the interface is deep, shining UV light at the interface locally increases the surface tension and, therefore, generates a surface flow that carries the marble towards the light source. Interestingly, they showed that the marble is transported in the opposite direction (i.e. away from the source of the UV light) at shallow enough water depths. The authors attributed their observation to the deformation of the interface. However, our findings suggest that, even if the interface deformation is a non-negligible factor, it may not be the sole contributor to the reported phenomenon.

Chapter 5: Summary and Future Directions

We studied the Marangoni-driven motion of active surfers located at a liquid-gas interface. We used both theory and numerical simulation to conduct our analyses. First, we derived an analytical expression for the propulsion speed in the absence of advective effects (i.e., when Re = Pe = 0). The derivation was based on the reciprocal theorem, which allowed us to bypass the detail calculation of the flow field. The analytical formula was used to theoretically examine the effect of confinement on the propulsion of oblate spheroidal surfers. We demonstrated that, depending on the geometry and degree of confinement, the surfing particles may propel forward in the higher surface tension direction or propel backward in the reverse direction. Knowing that the direction of propulsion is altered by a change in the surrounding boundary can be harnessed for designing smart surfing robots capable of sensing their environment. Combining the reciprocal theorem and with the method of singular perturbation expansion, we also calculated the leading-order corrections to the propulsion speed of Marangoni surfers due to advective effects resulting from finite Reynolds and Péclet numbers. Our calculations revealed that the speed increases with increasing Re and

Pe from zero.

Next, we developed a high-fidelity computational framework to further examine the Marangoni surfing. Two different approaches were adopted to capture the kinematics of the surfer. For pure translation, the governing equations were expressed in a non-inertial reference frame attached to the surfer and solved on a fixed nested mesh. For combined rotation and translation, however, the equations (again written in a frame of reference that moves, but not rotate, with the surfer) were solved on overset grids. We extensively tested the validity of the proposed numerical approach and showed that it is capable of faithfully simulating the Marangoni propulsion of active surfers.

We employed the validated simulations to perform three investigations. First, we studied the effects of the fluid inertia and advective transport of the released chemical agent on the propulsion behavior of various surfers. Our numerical calculations revealed that the normalized speed changes non-monotonically with the Reynolds and Péclet numbers. Specifically, we showed that there exist Re and Pe at which the speed is maximum. We also defined a new parameter that represents the "fuel efficiency" of the surfer. This parameter measures the ratio of the speed to the release rate of the active chemical. We found that the surfers reach their peak speed and fuel efficiency when $\mathrm{Re} \sim \mathrm{Pe} \sim \mathcal{O}(1)$.

We then analyzed the stability of a sphere translating along a liquid-gas interface. We demonstrated that, at the same speed, the sphere is more stable if it is self-driven

by Marangoni stresses compared to the case where it is dragged along the interface via an external force in the absence of any surface tension gradients. We inspected the vortical structures created in the wake of both Marangoni- and externally-driven spheres and found that the flow near the release site of the Marangoni surfer restricts the stretching of the vortices, which delays the onset of shedding and the consequent instability.

We finally investigated the propulsion characteristics of Marangoni surfers under confinement. We again confirmed that, contrary to what might be the usual expectation, the surfers may propel themselves in the direction of lower surface tension. This counterintuitive phenomenon emerges due to the competition between two opposing influences, namely, the net surface tension force acting along the three-phase contact line and the force exerted on the submerged area of the surfer by the flow in the bulk of the liquid layer, which is induced by the Marangoni stresses at the interface and the motion of the surfer itself. Perhaps surprisingly, we uncovered that a large percentage of the fluid force originates from the negative pressure acting on the active half of the surfer, and that this suction force is the main driving mechanism for the reverse Marangoni propulsion. We showed that, at low and intermediate Reynolds numbers (i.e., $Re \lessapprox 10$), there exists a critical gap size below which the surfers reverse course and move away from the higher surface tension region of their neighborhoods. Our calculations revealed that the existence of the critical gap at higher Reynolds numbers depends on the shape of the surfer, with a greater likelihood for thinner surfers.

Overall, the findings of this dissertation enhance the fundamental understanding of the Marangoni propulsion at liquid-gas interfaces. They also furnish much needed design guidelines for engineering Marangoni surfers with desired performance characteristics. Furthermore, the reported studies provide solid starting points for additional investigations into Marangoni propulsion. Interesting topics of future research may include exploring the effects of capillary forces and interface curvature on the propulsion speed and examining the collective motion of multiple surfers.

Bibliography

[1] M. Sitti, "Miniature devices: Voyage of the microrobots," *Nature*, vol. 458, no. 7242, pp. 1121–1122, 2009.

[2] M. Sitti, H. Ceylan, W. Hu, J. Giltinan, M. Turan, S. Yim, and E. Diller, "Biomedical applications of untethered mobile milli/microrobots," *Proc. IEEE*, vol. 103, no. 2, pp. 205–224, 2015.

[3] R. Dreyfus, J. Baudry, M. L. Roper, M. Fermigier, H. A. Stone, and J. Bibette, "Microscopic artificial swimmers," *Nature*, vol. 437, no. 7060, pp. 862–865, 2005.

[4] H. Masoud and A. Alexeev, "Modeling magnetic microcapsules that crawl in microchannels," *Soft Matter*, vol. 6, no. 4, pp. 794–799, 2010.

[5] H. Masoud, B. I. Bingham, and A. Alexeev, "Designing maneuverable micro-swimmers actuated by responsive gel," *Soft Matter*, vol. 8, no. 34, pp. 8944–8951, 2012.

[6] W. Wang, W. Duan, S. Ahmed, T. E. Mallouk, and A. Sen, "Small power: Autonomous nano-and micromotors propelled by self-generated gradients," *Nano Today*, vol. 8, no. 5, pp. 531–554, 2013.

[7] U. K. Cheang, F. Meshkati, D. Kim, M. J. Kim, and H. C. Fu, "Minimal geometric requirements for micropropulsion via magnetic rotation," *Phys. Rev. E*, vol. 90, no. 3, p. 033007, 2014.

[8] S. Sánchez, L. Soler, and J. Katuri, "Chemically powered micro-and nanomotors," *Angew. Chem. Int. Ed.*, vol. 54, no. 5, pp. 1414–1444, 2015.

[9] C. Maggi, F. Saglimbeni, M. Dipalo, F. De Angelis, and R. Di Leonardo, "Micromotors with asymmetric shape that efficiently convert light into work by thermocapillary effects," *Nat. Commun.*, vol. 6, p. 7855, 2015.

[10] W. Duan, W. Wang, S. Das, V. Yadav, T. E. Mallouk, and A. Sen, "Synthetic nano-and micromachines in analytical chemistry: Sensing, migration, capture, delivery, and separation," *Annu. Rev. Anal. Chem.*, vol. 8, pp. 311–333, 2015.

[11] K. K. Dey, F. Wong, A. Altemose, and A. Sen, "Catalytic motors–Quo Vadimus?" *Curr. Opin. Colloid Interface Sci.*, vol. 21, pp. 4–13, 2016.

[12] A. Domínguez, P. Malgaretti, M. N. Popescu, and S. Dietrich, "Effective interaction between active colloids and fluid interfaces induced by Marangoni flows," *Phys. Rev. Lett.*, vol. 116, p. 078301, Feb 2016.

[13] L. Rayleigh, "Measurements of the amount of oil necessary in order to check the motions of camphor upon water," *Proc. Royal Soc. Lond.*, vol. 47, no. 286-291, pp. 364–367, 1889.

[14] S. Nakata, Y. Iguchi, S. Ose, M. Kuboyama, T. Ishii, and K. Yoshikawa, "Self-rotation of a camphor scraping on water: new insight into the old problem," *Langmuir*, vol. 13, no. 16, pp. 4454–4458, 1997.

[15] N. Bassik, B. T. Abebe, and D. H. Gracias, "Solvent driven motion of lithographically fabricated gels," *Langmuir*, vol. 24, no. 21, pp. 12 158–12 163, 2008.

[16] S. Soh, M. Branicki, and B. A. Grzybowski, "Swarming in shallow waters," *J. Phys. Chem. Lett.*, vol. 2, no. 7, pp. 770–774, 2011.

[17] H. Li, L. Qiao, X. Liu, and C. Luo, "Fabrication and testing of a self-propelled, miniaturized pdms flotilla," *Microsyst. Technol.*, vol. 18, no. 9-10, pp. 1431–1444, 2012.

[18] L. Qiao, D. Xiao, F. K. Lu, and C. Luo, "Control of the radial motion of a self-propelled microboat through a side rudder," *Sens. Actuat. A*, vol. 188, pp. 359–366, 2012.

[19] R. Sharma, S. T. Chang, and O. D. Velev, "Gel-based self-propelling particles get programmed to dance," *Langmuir*, vol. 28, no. 26, pp. 10 128–10 135, 2012.

[20] G. Zhao and M. Pumera, "Liquid–liquid interface motion of a capsule motor powered by the interlayer Marangoni effect," *J. Phys. Chem. B*, vol. 116, no. 35, pp. 10 960–10 963, 2012.

[21] T. Bansagi Jr, M. M. Wrobel, S. K. Scott, and A. F. Taylor, "Motion and interaction of aspirin crystals at aqueous–air interfaces," *J. Phys. Chem. B*, vol. 117, no. 43, pp. 13 572–13 577, 2013.

[22] H. Zhang, W. Duan, L. Liu, and A. Sen, "Depolymerization-powered autonomous motors using biocompatible fuel," *J. Am. Chem. Soc.*, vol. 135, no. 42, pp. 15 734–15 737, 2013.

[23] M. Xiao, C. Jiang, and F. Shi, "Design of a uv-responsive microactuator on a smart device for light-induced on-off-on motion," *NPG Asia Mater.*, vol. 6, no. 9, p. e128, 2014.

[24] C. H. Ooi, A. Van Nguyen, G. M. Evans, O. Gendelman, E. Bormashenko, and N.-T. Nguyen, "A floating self-propelling liquid marble containing aqueous ethanol solutions," *RSC Adv.*, vol. 5, no. 122, pp. 101 006–101 012, 2015.

[25] J. E. Satterwhite-Warden, D. K. Kondepudi, J. A. Dixon, and J. F. Rusling, "Co-operative motion of multiple benzoquinone disks at the air–water interface," *Phys. Chem. Chem. Phys.*, vol. 17, no. 44, pp. 29 891–29 898, 2015.

[26] A. Srinivasan, J. Roche, V. Ravaine, and A. Kuhn, "Synthesis of conducting asymmetric hydrogel particles showing autonomous motion," *Soft Matter*, vol. 11, no. 20, pp. 3958–3962, 2015.

[27] I. L. Liakos, P. Salvagnini, A. Scarpellini, R. Carzino, C. Beltran, E. Mele, V. Murino, and A. Athanassiou, "Biomimetic locomotion on water of a porous

natural polymeric composite," *Adv. Mater. Interfaces*, vol. 3, no. 11, p. 1500854, 2016.

[28] R. Sharma, T. E. Corcoran, S. Garoff, T. M. Przybycien, and R. D. Tilton, "Transport of a partially wetted particle at the liquid/vapor interface under the influence of an externally imposed surfactant generated Marangoni stress," *Colloids Surf. A*, vol. 521, pp. 49–60, 2017.

[29] S. K. Srivastava and O. G. Schmidt, "Autonomously propelled motors for value-added product synthesis and purification," *Chem.: Eur. J.*, vol. 22, no. 27, pp. 9072–9076, 2016.

[30] A. Musin, R. Grynyov, M. Frenkel, and E. Bormashenko, "Self-propulsion of a metallic superoleophobic micro-boat," *J. Colloid Interface Sci.*, vol. 479, pp. 182–188, 2016.

[31] R. Fernandes and D. H. Gracias, "Toward a miniaturized mechanical surgeon," *Mater. Today*, vol. 12, no. 10, pp. 14–20, 2009.

[32] N. M. Andersen, *A Comparative Study of Locomotion on the Water Surface in Semiaquatic Bugs (Insecta, Hemiptera, Gerromorpha).* Vidensk Meddr Dansk Naturh Foren, 1976.

[33] H. Schildknecht, "Chemical ecology–a chapter of modern natural products chemistry," *Angew. Chem. Int. Ed.*, vol. 15, no. 4, pp. 214–222, 1976.

[34] K. E. Linsenmair and R. Jander, "Das "entspannungsschwimmen" von velia und stenus," *Sci. Nat.*, vol. 50, no. 6, pp. 231–231, 1963.

[35] J. W. M. Bush and D. L. Hu, "Walking on water: biolocomotion at the interface," *Annu. Rev. Fluid Mech.*, vol. 38, pp. 339–369, 2006.

[36] R. Daniels, S. Reynaert, H. Hoekstra, C. Verreth, J. Janssens, K. Braeken, M. Fauvart, S. Beullens, C. Heusdens, I. Lambrichts, D. E. De Vos, J. Vanderleyden, J. Vermant, and J. Michiels, "Quorum signal molecules as biosurfactants affecting swarming in Rhizobium etli," *Proc. Natl. Acad. Sci. U. S. A.*, vol. 103, no. 40, pp. 14 965–14 970, 2006.

[37] T. E. Angelini, M. Roper, R. Kolter, D. A. Weitz, and M. P. Brenner, "Bacillus subtilis spreads by surfing on waves of surfactant," *Proc. Natl. Acad. Sci. U. S. A.*, vol. 106, no. 43, pp. 18 109–18 113, 2009.

[38] D. B. Kearns, "A field guide to bacterial swarming motility," *Nat. Rev. Microbiol.*, vol. 8, no. 9, pp. 634–644, 2010.

[39] M. Fauvart, P. Phillips, D. Bachaspatimayum, N. Verstraeten, J. Fransaer, J. Michiels, and J. Vermant, "Surface tension gradient control of bacterial swarming in colonies of Pseudomonas aeruginosa," *Soft Matter*, vol. 8, no. 1, pp. 70–76, 2012.

[40] J. W. Bush, D. L. Hu, and M. Prakash, "The integument of water-walking arthropods: form and function," *Advances in insect physiology*, vol. 34, pp. 117–192, 2007.

[41] H. Kitahata, S.-I. Hiromatsu, Y. Doi, S. Nakata, and M. R. Islam, "Self-motion of a camphor disk coupled with convection," *Phys. Chem. Chem. Phys.*, vol. 6, no. 9, pp. 2409–2414, 2004.

[42] S. Soh, K. J. Bishop, and B. A. Grzybowski, "Dynamic self-assembly in ensembles of camphor boats," *J. Phys. Chem. B*, vol. 112, no. 35, pp. 10 848–10 853, 2008.

[43] S. Nakata and M. Murakami, "Self-motion of a camphor disk on an aqueous phase depending on the alkyl chain length of sulfate surfactants," *Langmuir*, vol. 26, no. 4, pp. 2414–2417, 2009.

[44] Y. Shibuya and S. Matsushita, "Electric current generation by camphor boats," *Mol. Cryst. Liq. Cryst.*, vol. 504, no. 1, pp. 27–34, 2009.

[45] N. J. Suematsu, S. Nakata, A. Awazu, and H. Nishimori, "Collective behavior of inanimate boats," *Phys. Rev. E*, vol. 81, no. 5, p. 056210, 2010.

[46] E. Heisler, N. J. Suematsu, A. Awazu, and H. Nishimori, "Collective motion and phase transitions of symmetric camphor boats," *J. Phys. Soc. Jpn.*, vol. 81, no. 7, p. 074605, 2012.

[47] C. Luo, H. Li, L. Qiao, and X. Liu, "Development of surface tension-driven microboats and microflotillas," *Microsyst. Technol.*, vol. 18, no. 9-10, pp. 1525–1541, 2012.

[48] E. Lauga and A. M. J. Davis, "Viscous Marangoni propulsion," *J. Fluid Mech.*, vol. 705, pp. 120–133, 2012.

[49] H. Kitahata, K. Iida, and M. Nagayama, "Spontaneous motion of an elliptic camphor particle," *Phys. Rev. E*, vol. 87, no. 1, p. 010901, 2013.

[50] V. Pimienta and C. Antoine, "Self-propulsion on liquid surfaces," *Curr. Opin. Colloid Interface Sci.*, vol. 19, no. 4, pp. 290–299, 2014.

[51] A. Würger, "Thermally driven Marangoni surfers," *J. Fluid Mech.*, vol. 752, pp. 589–601, 2014.

[52] H. Masoud and H. A. Stone, "A reciprocal theorem for Marangoni propulsion," *J. Fluid Mech.*, vol. 741, p. R4, 2014.

[53] H. Masoud and M. J. Shelley, "Collective surfing of chemically active particles," *Phys. Rev. Lett.*, vol. 112, p. 128304, 2014.

[54] K. Iida, H. Kitahata, and M. Nagayama, "Theoretical study on the translation and rotation of an elliptic camphor particle," *Phys. D*, vol. 272, pp. 39–50, 2014.

[55] K. Nishi, K. Wakai, T. Ueda, M. Yoshii, Y. S. Ikura, H. Nishimori, S. Nakata, and M. Nagayama, "Bifurcation phenomena of two self-propelled camphor disks on an annular field depending on system length," *Phys. Rev. E*, vol. 92, no. 2, p. 022910, 2015.

[56] N. J. Suematsu, K. Tateno, S. Nakata, and H. Nishimori, "Synchronized intermittent motion induced by the interaction between camphor disks," *J. Phys. Soc. Jpn.*, vol. 84, no. 3, p. 034802, 2015.

[57] L. Wang, B. Yuan, J. Lu, S. Tan, F. Liu, L. Yu, Z. He, and J. Liu, "Self-propelled and long-time transport motion of PVC particles on a water surface," *Adv. Mater.*, vol. 28, no. 21, pp. 4065–4070, 2016.

[58] A. Girot, N. Danné, A. Würger, T. Bickel, F. Ren, J. C. Loudet, and B. Pouligny, "Motion of optically heated spheres at the water-air interface," *Langmuir*, vol. 32, no. 11, pp. 2687–2697, 2016.

[59] A. Dominguez, P. Malgaretti, M. N. Popescu, and S. Dietrich, "Effective interaction between active colloids and fluid interfaces induced by Marangoni flows," *Phys. Rev. Lett.*, vol. 116, no. 7, p. 078301, 2016.

[60] M. Frenkel, G. Whyman, E. Shulzinger, A. Starostin, and E. Bormashenko, "Self-propelling rotator driven by soluto-capillary marangoni flows," *Appl. Phys. Lett.*, vol. 110, no. 13, p. 131604, 2017.

[61] M. Frenkel, V. Multanen, R. Grynyov, A. Musin, Y. Bormashenko, and E. Bormashenko, "Camphor-engine-driven micro-boat guides evolution of chemical gardens," *Sci. Rep.*, vol. 7, no. 1, p. 3930, 2017.

[62] W. Fei, Y. Gu, and K. J. Bishop, "Active colloidal particles at fluid-fluid interfaces," *Curr. Opin. Colloid Interface Sci.*, vol. 32, pp. 57–68, 2017.

[63] H. Nishimori, N. J. Suematsu, and S. Nakata, "Collective behavior of camphor floats migrating on the water surface," *J. Phys. Soc. Jpn.*, vol. 86, no. 10, p. 101012, 2017.

[64] Y. Koyano, M. Gryciuk, P. Skrobanska, M. Malecki, Y. Sumino, H. Kitahata, and J. Gorecki, "Relationship between the size of a camphor-driven rotor and its angular velocity," *Phys. Rev. E*, vol. 96, no. 1, p. 012609, 2017.

[65] A. Domínguez and M. N. Popescu, "Phase coexistence in a monolayer of active particles induced by marangoni flows," *Soft Matter*, vol. 14, no. 39, pp. 8017–8029, 2018.

[66] M. Frenkel, A. Vilk, I. Legchenkova, S. Shoval, and E. Bormashenko, "Mini-generator of electrical power exploiting the Marangoni flow inspired self-propulsion," *ACS Omega*, vol. 4, no. 12, pp. 15 265–15 268, 2019.

[67] H. Morohashi, M. Imai, and T. Toyota, "Construction of a chemical motor-movable frame assembly based on camphor grains using water-floating 3d-printed models," *Chem. Phys. Lett.*, vol. 721, pp. 104–110, 2019.

[68] H. Gidituri, M. V. Panchagnula, and A. Pototsky, "Dynamics of a fully wetted Marangoni surfer at the fluid–fluid interface," *Soft Matter*, vol. 15, no. 10, pp. 2284–2291, 2019.

[69] R. J. Löffler, M. M. Hanczyc, and J. Gorecki, "A hybrid camphor-camphene wax material for studies on self-propelled motion," *Phys. Chem. Chem. Phys.*, vol. 21, no. 45, pp. 24 852–24 856, 2019.

[70] S. Sur, H. Masoud, and J. P. Rothstein, "Translational and rotational motion of disk-shaped Marangoni surfers," *Phys. Fluids*, vol. 31, no. 10, p. 102101, 2019.

[71] K. Dietrich, N. Jaensson, I. Buttinoni, G. Volpe, and L. Isa, "Microscale marangoni surfers," *Phys. Rev. Lett.*, vol. 125, no. 9, p. 098001, 2020.

[72] H. Masoud and H. A. Stone, "The reciprocal theorem in fluid dynamics and transport phenomena," *J. Fluid Mech.*, vol. 879, p. P1, 2019.

[73] M. E. O'Neill, K. B. Ranger, and H. Brenner, "Slip at the surface of a translating–rotating sphere bisected by a free surface bounding a semi-infinite viscous fluid: Removal of the contact-line singularity," *Phys. Fluids*, vol. 29, no. 4, pp. 913–924, 1986.

[74] C. Pozrikidis, "Particle motion near and inside an interface," *J. Fluid Mech.*, vol. 575, pp. 333–357, 2007.

[75] P. Ganatos, R. Pfeffer, and S. Weinbaum, "A strong interaction theory for the creeping motion of a sphere between plane parallel boundaries. part 2. parallel motion," *J. Fluid Mech.*, vol. 99, no. 04, pp. 755–783, 1980.

[76] A. M. J. Davis, "Slow viscous flow due to motion of an annular disk; pressure-driven extrusion through an annular hole in a wall," *J. Fluid Mech.*, vol. 231, pp. 51–71, 1991.

[77] W. E. Acree, "Empirical expression for predicting surface-tension of liquid-mixtures," *J. Colloid Interface Sci.*, vol. 101, pp. 575–576, 1984.

[78] A. W. Adamson, *Physical Chemistry of Surfaces*. New York: Wiley, 1990.

[79] H. A. Stone and H. Masoud, "Mobility of membrane-trapped particles," *J. Fluid Mech.*, vol. 781, pp. 494–505, 2015.

[80] J. R. Blake, "A note on the image system for a Stokeslet in a no-slip boundary," *Math. Proc. Camb. Philos. Soc.*, vol. 70, no. 02, pp. 303–310, 1971.

[81] S. J. Kang, S. Sur, J. P. Rothstein, and H. Masoud, "Forward, reverse, and no motion of marangoni surfers under confinement," *Physical Review Fluids*, vol. 5, no. 8, p. 084004, 2020.

[82] F. Moukalled, L. Mangani, and M. Darwish, *The Finite Volume Method in Computational Fluid Dynamics: An Advanced Introduction with OpenFOAM® and Matlab®*. Springer, 2015, vol. 113.

[83] C. Pozrikidis, *Introduction to Theoretical and Computational Fluid Dynamics*. Oxford: Oxford university press, 2011.

[84] B. E. Griffith and N. A. Patankar, "Immersed methods for fluid–structure interaction," *Annu. Rev. Fluid Mech.*, vol. 52, 2020.

[85] C. J. Freitas and S. R. Runnels, "Simulation of fluid–structure interaction using patched-overset grids," *J. Fluid. Struct.*, vol. 13, no. 2, pp. 191–207, 1999.

[86] W. M. Chan, "Overset grid technology development at nasa ames research center," *Comput. Fluids*, vol. 38, no. 3, pp. 496–503, 2009.

[87] H. S. Tang, S. C. Jones, and F. Sotiropoulos, "An overset-grid method for 3d unsteady incompressible flows," *J. Comput. Phys.*, vol. 191, no. 2, pp. 567–600, 2003.

[88] H.-B. Deng, Y.-Q. Xu, D.-D. Chen, H. Dai, J. Wu, and F.-B. Tian, "On numerical modeling of animal swimming and flight," *Comput. Mech.*, vol. 52, no. 6, pp. 1221–1242, 2013.

[89] Z. Shen, D. Wan, and P. M. Carrica, "Dynamic overset grids in openfoam with application to kcs self-propulsion and maneuvering," *Ocean Eng.*, vol. 108, pp. 287–306, 2015.

[90] R. Meakin, "Moving body overset grid methods for complete aircraft tiltrotor simulations," in *11th Computational Fluid Dynamics Conference*, 1993, p. 3350.

[91] J. L. Steger, F. C. Dougherty, and J. A. Benek, "A chimera grid scheme.[multiple overset body-conforming mesh system for finite difference adaptation to complex aircraft configurations]," 1983.

[92] B. Hubbard and H.-C. Chen, "A chimera scheme for incompressible viscous flows with application to submarine hydrodynamics," in *Fluid Dynamics Conference*, 1994, p. 2210.

[93] G. Chesshire and W. D. Henshaw, "Composite overlapping meshes for the solution of partial differential equations," *J. Comput. Phys.*, vol. 90, no. 1, pp. 1–64, 1990.

[94] W. D. Henshaw and D. W. Schwendeman, "Parallel computation of three-dimensional flows using overlapping grids with adaptive mesh refinement," *J. Comput. Phys.*, vol. 227, no. 16, pp. 7469–7502, 2008.

[95] W. D. Henshaw, "Adaptive mesh and overlapping grid methods," *Ency. Aerosp. Eng.*, 2010.

[96] S. E. Sherer and J. N. Scott, "High-order compact finite-difference methods on general overset grids," *J. Comput. Phys.*, vol. 210, no. 2, pp. 459–496, 2005.

[97] A. Sane, S. Mandre, and I. Kim, "Surface tension of flowing soap films," *J. Fluid Mech.*, vol. 841, p. R2, 2018.

[98] N. Kavokine, M. Anyfantakis, M. Morel, S. Rudiuk, T. Bickel, and D. Baigl, "Light-driven transport of a liquid marble with and against surface flows," *Angew. Chem. Int. Ed.*, vol. 55, no. 37, pp. 11 183–11 187, 2016.